

¹ Study of the multi-strange resonance $\Xi(1530)^0$ production
² with ALICE at the LHC energies

³ Jihye Song

4 Contents

5	List of Figures	4
6	List of Tables	8
7	1 The physics of relativistic heavy-ion collisions	9
8	1.1 Standard model	9
9	1.2 Quantum Chromo-Dynamics	10
10	1.3 Heavy Ion Collisions	13
11	2 Production of resonance with strangeness	15
12	2.1 Resonance with strangeness	15
13	3 Theoretical models	15
14	3.1 Thermal statistical model	15
15	3.1.1 Calculations	17
16	3.1.2 Results	17
17	3.1.3 Comparison with data	19
18	3.2 UrQMD	19
19	4 A Large Ion Collider Experiment at the LHC	20
20	4.1 The Large Hadron Collider	20
21	4.2 The ALICE project	23
22	4.2.1 ALICE detector	23
23	4.2.2 Data Acquisition (DAQ) and trigger system	33
24	4.2.3 ALICE offline software frame work	35
25	5 Measurement of $\Xi(1530)^0$ production in p-Pb and Pb-Pb	37
26	5.1 $\Xi(1530)^0$ -reconstruction	37
27	5.1.1 Data sample and event selection	37
28	5.1.2 Track and topological selection	41
29	5.1.3 Particle identification	44
30	5.1.4 Signal extraction	47
31	5.2 Efficiency correction	56
32	5.3 Corrected p_T -spectra	59
33	5.4 Systematic uncertainties	61
34	5.5 $\Xi(1530)^0$ transverse momentum spectra	66
35	6 Further results and discussion	69
36	6.1 Mean transverse momentum	69
37	6.2 Particle yield ratios	73

38	6.2.1 Integrated yield ratios of excited to ground-state hadrons	73
39	6.3 Integrated yield ratios to pion	76
40	References	80

⁴¹ **List of Figures**

42	1	Standard Model families of leptons and quarks as the gauge bosons	9
43	2	Summary of measurements of τ s as a function of the respective energy scale Q. The respective degree of QCD perturbation theory used in the extraction of τ s is indicated in brackets (NLO: next-to-leading order; NNLO: next-to-next-to leading order; res. NNLO: NNLO matched with resummed next-to-leading logs; N3LO: next-to-NNLO) [1]	12
44	3	Hydrodynamic evolution of a heavy ion collision with and without the formation of a QGP.	14
45	4	Ratio of baryonic and mesonic resonances over their stable partner as a function of temperature.	18
46	5	Ratio of resonances over their stable partner as a function of $\sqrt(s)$	19
47	6	The CERN accelerator complex [2]	21
48	7	The ALICE detector	25
49	8	Schematic view of the ITS [3]	26
50	9	Track impact parameter resolution in the transverse plane ($r\phi$) vs p_T for charged particle	27
51	10	Schematic view of the TPC	28
52	11	Specific energy loss (dE/dx) in the TPC vs. particle momentum in Pb–Pb collisions at $\sqrt{s_{NN}} = 2.76$ TeV. The lines show the parametrisations of the expected mean energy loss.	29
53	12	Correlation between the sum and difference of signal times in V0A and V0C. Three classes of events collisions at (8.3 ns, 14.3 ns), background from Beam 1 at (-14.3 ns, -8.3 ns), and background from Beam 2 at (14.3 ns, 8.3 ns) can be clearly distinguished.	31
54	13	Distribution of the V0 amplitude (sum of V0A and V0C in top, V0A in bottom). The inset shows a magnified version of the most peripheral region.	32
55	14	The overall architecture of the ALICE DAQ and the interface to the HLT system.	33
56	15	Schematic view of the AliRoot framework	36
57	16	Vertex-z coordinate distribution of the accepted events in p–Pb collision(Left) and in Pb–Pb collisions(Right). The red dashed line indicates vertex cut	39
58	17	Multiplicity distribution of accepted events in p–Pb collision in percentile. The each color and labels define the four intervals in which the analysis is performed.	39
59	18	Centrality distribution of three different trigger classes.	40
60	19	Sketch of the decay modes for Ξ^{*0} and depiction of the track and topological selection criteria.	42
61	20	TPC dE/dx as function of transverse momentum for total (top) and selected first emitted π in 3σ (bottom)	44

81	21	TPC dE/dx as function of transverse momentum for total (top) and selected second emitted π in 3σ (bottom)	44
83	22	TPC dE/dx as function of transverse momentum for total (top) and selected last emitted π in 3σ (bottom)	45
85	23	TPC dE/dx as function of transverse momentum for total (top) and selected proton in 3σ (bottom)	45
87	24	TPC dE/dx as function of transverse momentum for total (top) and selected first emitted π in 3σ (bottom)	45
89	25	TPC dE/dx as function of transverse momentum for total (top) and selected second emitted π in 3σ (bottom)	46
91	26	TPC dE/dx as function of transverse momentum for total (top) and selected last emitted π in 3σ (bottom)	46
93	27	TPC dE/dx as function of transverse momentum for total (top) and selected proton in 3σ (bottom)	47
95	28	The $\Xi^\mp\pi^\pm$ invariant mass distribution (Same-event pairs) in $1.8 < p_T < 2.2 \text{ GeV}/c$ and for the multiplicity class 20-40%. The background shape, using pairs from different events (Mixed-event background), is normalised to the counts in $1.49 < M_{\Xi\pi} < 1.51 \text{ GeV}/c^2$ and $1.56 < M_{\Xi\pi} < 1.58 \text{ GeV}/c^2$	48
99	29	The $\Xi^\mp\pi^\pm$ invariant mass distribution (Same-event pairs) in $3.0 < p_T < 3.5 \text{ GeV}/c$ and for the centrality class 0-10%. The background shape, using pairs from different events (Mixed-event background), is normalised to the counts in $1.49 < M_{\Xi\pi} < 1.51 \text{ GeV}/c^2$ and $1.56 < M_{\Xi\pi} < 1.58 \text{ GeV}/c^2$	49
101	30	The invariant mass distribution after subtraction of the mixed-event background in p–Pb collisions. The solid curve represents the combined fit, while the dashed line describes the residual background.	50
103	31	The invariant mass distribution after subtraction of the mixed-event background in Pb–Pb collisions. The solid curve represents the combined fit, while the dashed line describes the residual background.	51
105	32	σ fit parameters as a function of p_T in MB in p–Pb collisions (top) and in Pb–Pb collisions (bottom).	53
107	33	$\Xi(1530)^0$ -mass obtained from fit of the Voigtian peak as a function of p_T in each multiplicity classes in p–Pb collisions (top) and the different centrality classes in Pb–Pb (bottom).	54
109	34	$\Xi(1530)^0$ -raw spectra obtained from fit of the Voigtian peak and a polynomial residual background for different multiplicities in p–Pb collisions (top) and Pb–Pb collisions (bottom). Only the statistical error is reported.	55
111	35	$\Xi(1530)^0$ -raw spectra obtained from fit of the Voigtian peak and a polynomial residual background for different multiplicities. Only the statistical error is reported.	56

120	36	Real corrected $\Xi(1530)^0$ spectrum (black) for the minimum bias with Levy fit (black curve). Also shown are the unweighted generated (blue) and reconstructed (red) $\Xi(1530)^0$ spectra.	57
121	37	Efficiency as a function of p_{T} in minimum bias events in p–Pb collisions.	58
122	38	Efficiency as a function of p_{T} in different centrality classes in Pb–Pb collisions	59
123	39	Corrected p_{T} -spectra of $\Xi(1530)^0$ in NSD and different multiplicity classes in p–Pb collisions.	60
124	40	Corrected p_{T} -spectra of $\Xi(1530)^0$ in different centrality classes in Pb–Pb collisions.	60
125	41	Summary of the contributions to the systematic uncertainty in minimum bias events in p–Pb collisions. The dashed black line is the sum in quadrature of all the contributions.	64
126	42	Systematic uncertainties for each multiplicity classes in p–Pb collisions.	64
127	43	Summary of the contributions to the systematic uncertainty in minimum bias events in Pb–Pb collisions. The dashed black line is the sum in quadrature of all the contributions.	65
128	44	Systematic uncertainties for each multiplicity classes.	65
129	45	Corrected yields as function of p_{T} in NSD events and multiplicity dependent event classes in p–Pb collision system. Statistical uncertainties are presented as bar and systematical uncertainties are plotted as boxes.	67
130	46	Corrected yields as function of p_{T} in different centrality classes in Pb–Pb collision system. Statistical uncertainties are presented as bar and systematical uncertainties are plotted as boxes.	68
131	47	Mean transverse momenta $\langle p_{\text{T}} \rangle$ of Λ , Ξ^- , $\Sigma^{*\pm}$, Ξ^{*0} and Ω^- in p–Pb collisions at $\sqrt{s_{\text{NN}}} = 5.02$ TeV as a function of mean charged-particle multiplicity density $\langle dN_{\text{ch}}/d\eta_{\text{lab}} \rangle$, measured in the pseudorapidity range $ \eta_{\text{lab}} < 0.5$. The results for Λ , Ξ^- and Ω^- are taken from [4, 5, 6]. Statistical and systematic uncertainties are represented as bars and boxes, respectively. The Ω^- and Ξ^- points in the 3rd and 4th lowest multiplicity bins are slightly displaced along the abscissa to avoid superposition with the $\Xi(1530)^0$ points.	70
132	48	Mass dependence of the mean transverse momenta of identified particles for the 0 – 20% V0A multiplicity class and with $-0.5 < y_{\text{CMS}} < 0$ in p–Pb collisions at $\sqrt{s_{\text{NN}}} = 5.02$ TeV [4, 6], and in minimum-bias pp collisions at $\sqrt{s} = 7$ TeV [7] with $ y_{\text{CMS}} < 0.5$. Additionally, D^0 and J/ψ results are plotted. The D^0 and J/ψ were measured in different rapidity ranges: $ y_{\text{CMS}} < 0.5$ [8] ($ y_{\text{CMS}} < 0.9$ [9]) for D^0 (J/ψ) in pp and $-0.96 < y_{\text{CMS}} < 0.04$ [8] ($-1.37 < y_{\text{CMS}} < 0.43$ [10]) for D^0 (J/ψ) in p–Pb. Note also that the results for D^0 and J/ψ in p–Pb collisions are for the 0–100% multiplicity class.	71

159	49	Ratio of $\Xi(1530)^0$ to Ξ^- measured in pp [7], p–Pb [4, 6] and Pb–Pb collisions as a function of $\langle dN_{ch}/d\eta_{lab} \rangle$ measured at midrapidity. Statistical uncertainties (bars) are shown as well as total systematic uncertainties (hollow boxes) and systematic uncertainties uncorrelated across multiplicity (shaded boxes). A few model predictions are also shown as lines at their appropriate abscissa.	74
160			
161			
162			
163			
164			
165	50	Ratio of $\rho/\pi(U_p)$, K^*/K , $\phi/K(\text{Left bottom})$ and Λ^*/Λ with system size measured at mid-rapidity. Statistical uncertainties (bars) are shown as well as total systematic uncertainties (hollow boxes) and systematic uncertainties uncorrelated across multiplicity (shaded boxes). A few model predictions are also shown as lines at their appropriate abscissa.	75
166			
167			
168			
169			
170	51	Ratio of $\Xi(1530)^0$ to π^\pm , measured in pp [11] and p–Pb [7] collisions, as a function of the average charged particle density ($\langle dN_{ch}/d\eta_{lab} \rangle$) measured at mid-rapidity. Statistical uncertainties (bars) are shown as well as total systematic uncertainties (hollow boxes) and systematic uncertainties uncorrelated across multiplicity (shaded boxes). A few model predictions are also shown as lines at their appropriate abscissa.	77
171			
172			
173			
174			
175			
176	52	Particle yield ratios to pions of strange and multi-strange hadrons normalized to the values measured in pp collisions, both in pp and in p–Pb collisions. The common systematic uncertainties cancel in the double-ratio. The empty boxes represent the remaining uncorrelated uncertainties. The lines represent a simultaneous fit of the results with the empirical scaling formula in Equation ??..	78
177			
178			
179			
180			
181			
182	53	p_T -integrated yield ratios of strange and multi-strange hadrons to $(\pi^+ + \pi^-)$ as a function of $\langle dN_{ch}/d\eta_{lab} \rangle$ measured in the rapidity interval $ \eta < 0.5$. The empty and dark-shaded boxes show the total systematic uncertainty and the contribution uncorrelated across multiplicity bins, respectively. The values are compared to calculations from MC models and to results obtained in Pb–Pb and p–Pb collisions at the LHC.	79
183			
184			
185			
186			
187			

¹⁸⁸ **List of Tables**

¹⁸⁹	1	Parameters used in the thermal-model calculations.	16
¹⁹⁰	2	Properties of particles used in the ratio calculations.	17
¹⁹¹	3	Difference of mass (ΔM), baryon number (ΔB), strangeness (ΔS) and charge (ΔQ) of the ratios. The values of the slopes needs to be checked!!!! .	19
¹⁹²	4	Number of accepted and analyzed events per multiplicity/centrality interval	41
¹⁹³	5	Track selections common to all decay daughters and primary track selections applied to the charged pions from decays of Ξ^{*0}	41
¹⁹⁴	6	Topological and track selection criteria.	42
¹⁹⁵	7	Summary of the systematic uncertainties on the differential yield, $d^2N/(dp_T dy)$. Minimum and maximum values in all p_T intervals and multiplicity classes in p–Pb, centrality classes in Pb–Pb are shown for each source.	66
¹⁹⁶			
¹⁹⁷			
¹⁹⁸			
¹⁹⁹			

200 1 The physics of relativistic heavy-ion collisions

201 1.1 Standard model

202 . Our current understanding concerning the question what the world is made of is collected
 203 in the Standard Model of particle physics (SM) [12], that describes our universe in terms of
 204 matter and forces. In this picture matter is composed of 12 point-like particles, which have a
 205 spin of 1/2 (fermions) and can be classified according to how they interact or equivalently to
 206 what charges they carry. There are six quarks (up, down, charm, strange, top and bottom)
 207 and six leptons (electron, electron neutrino, muon, muon neutrino, tau, tau neutrino) as
 208 reported in Figure reffig:sm. The interactions between elementary particles are described
 209 by the exchange of gauge bosons (usually as virtual particles¹) or equivalently by mean of
 210 a field. Mathematically, the SM is a quantized Yang-Mills theory based on the non-abelian
 211 symmetry group $U(1) \rightarrow SU(2) \rightarrow SU(3)$ and has a total of twelve gauge bosons: the photon,
 212 three weak bosons and eight gluons. The interactions included in such a model are the
 213 electromagnetic force, the weak force and the strong one. Quarks have a property called
 214 color, playing the role of charge in the strong force. Both quarks and leptons are affected
 215 by the weak force and all the charged particles interact electromagnetically. The models
 216 that describe these interactions are listed as follows:

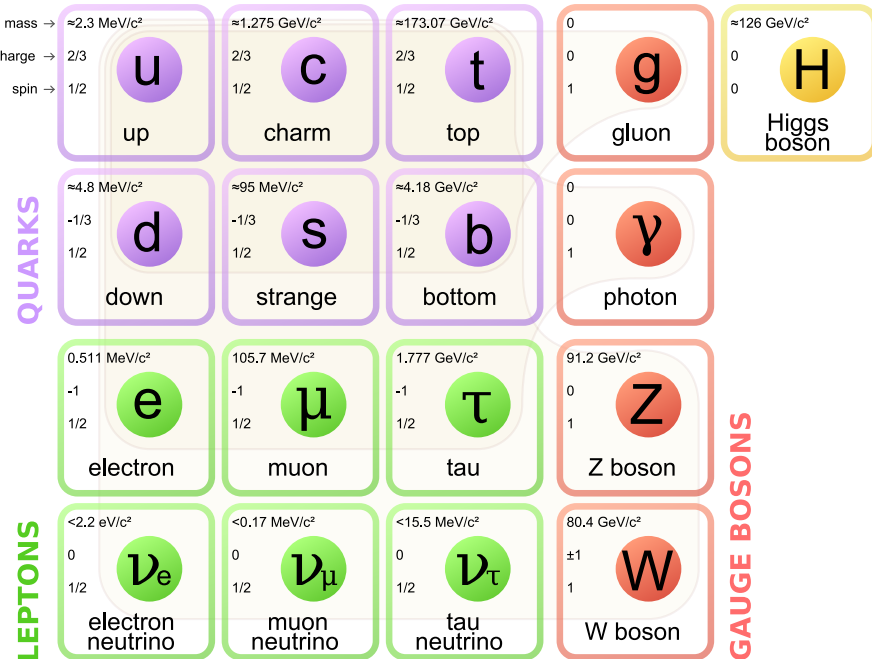


Figure 1: Standard Model families of leptons and quarks as the gauge bosons

217 **1.2 Quantum Chromo-Dynamics**

218 The strong interaction is one of the four fundamental forces in nature, together with gravity,
 219 electromagnetism and the weak interaction. Its existence was postulated in the 1970s,
 220 to explain how the atomic nucleus was bound together despite the protons? mutual electro-
 221 magnetic repulsion. This hypothesized force was called the strong force, which was believed
 222 to be a fundamental force that acted on the nucleons. It was later discovered that protons
 223 and neutrons were not fundamental particles, by means of deep inelastic experiments, but
 224 were made up of constituent particles (the quarks). The strong attraction between nucleons
 225 was the side-effect of a more fundamental force that bounds the quarks together in the pro-
 226 tons and neutrons. Nowadays the strong inter- action is described through the formalism
 227 of a Quantum Field Theory. The particular theory describing this force is the Quantum
 228 Chromo-Dynamics (QCD), in analogy to the Quantum Electro-Dynamics (QED) that de-
 229 scribes the electromagnetic interaction. In QED the electromagnetic force is mediated by
 230 photons, which carry no charge. Similarly, in QCD the gluons are the carriers of the strong
 231 force, but unlike the photon they carry color charge, meaning that they can interact with
 232 each other. In QED, the electrodynamic coupling constant is $\alpha = 1/137$, whereas the QCD
 233 strong coupling constant, α_s , can be 1 or larger. In quantum field theory when a coupling
 234 constant is much smaller than 1 the theory is said to be weakly coupled. When the coupling
 235 nears 1 the theory is strongly coupled, hence the name ?strong? force. In QCD the strong
 236 interaction between two quarks can be described using the following potential:

$$V(r) = -4\frac{\alpha_s}{3r} + kr \quad (1)$$

237 where r is the separation distance between the two quarks, α_s is the strong coupling
 238 constant, and k is also a constant that is approximately 1 GeV/fm. The renormalization
 239 scale dependence of the effective QCD coupling $\alpha_s = g_s^2/4\pi$ is controlled by the β -function:

$$\mu \frac{d\alpha_s}{d\mu} = 2\beta(\alpha_s) = -\frac{\beta_0}{2\pi}\alpha_s^2 - \frac{\beta_1}{4\pi^2}\alpha_s^3 - \frac{\beta_2}{64\pi^3}\alpha_s^4 - \dots \quad (2)$$

240 where

$$\beta_0 = 11 - \frac{2}{3}n_f \quad (3)$$

$$\beta_1 = 51 - \frac{19}{3}n_f \quad (4)$$

$$\beta_2 = 2857 - \frac{5033}{9}n_f + \frac{325}{27}n_f^2 \quad (5)$$

243 Here n_f is the number of quarks with mass less than the energy scale μ . In solving
 244 the differential equation 2 for α_s , a constant of integration is introduced. This constant is
 245 the fundamental constant of QCD that must de determined from experiment in addition
 246 to the quark masses. The most sensible choice for this constant is the value of α_s at a

247 fixed-reference scale μ_0 . It has become standard to choose $\mu_0 = M_Z$. At different values
248 of μ , α_s can be obtained from

$$\log\left(\frac{\mu^2}{\mu_0^2}\right) = \int_{\alpha_s(\mu_0)}^{\alpha_s(\mu)} \frac{d\alpha}{\beta(\alpha)} \quad (6)$$

249 It is also convenient to introduce the dimensional parameter $\Lambda[\text{MeV}^{-1}]$, since it provides
250 a parameterization of the μ dependence of α_s . The definition of Λ is arbitrary. One way to
251 define it is to write the solution of Equation 2 as an expansion in inverse power of $\ln(\mu^2)$:

$$\alpha_s = \frac{4\pi}{\beta_0 \ln(\mu^2/\Lambda^2)} \left[1 - \frac{2\beta_1}{\beta_0^2} \frac{\ln[\ln(\mu^2/\Lambda^2)]}{\ln(\mu^2/\Lambda^2)} + \frac{4\beta_1^2}{\beta_0^4 \ln^2(\mu^2/\Lambda^2)} \times ((\ln[\ln(\mu^2/\Lambda^2)]) - \frac{1}{2})^2 + \frac{\beta_2 \beta_0}{8\beta_1} - \frac{5}{4} \right] \quad (7)$$

252 Experimentally, α_s has been measured at different scales (μ). Figure 2 shows the
253 measurement of α_s as a function of the respective energy scale Q compared to the lattice
254 QCD calculation. Three very important properties of QCD arise from the running constant
255 α_s . They are confinement, asymptotic freedom, and (hidden) chiral symmetry. For large
256 distance scales the second term in the potential equation (Equation 7) dominates. This
257 means that the coupling between the two quarks is large, making it so that no free quarks
258 are observed in nature, i.e. a quark never exists on its own for longer than $1/\Lambda_{\text{QCD}}$, where
259 $\Lambda_{\text{QCD}} = 217 \text{ MeV}$. The up, down, strange, charm, and bottom quarks all hadronize on
260 the time-scale $1/\Lambda_{\text{QCD}}$, the top quark decays before it has time to hadronize. Therefore,
261 all but the top quark will be confined inside hadrons. Experimentally, no single quark in a
262 color- triplet state has ever been observed. Asymptotic freedom arises when the quarks are
263 at a small distance from one another or with a large enough momentum transfer Q ($\alpha_s \rightarrow$
264 0 as $\mu \rightarrow \infty$). The potential will go like $1/r$ and the effective coupling between the quarks
265 decreases, allowing for a quasi-free quark. The third property is called chiral symmetry,
266 also not observed in nature. It is a symmetry of QCD in the limit of vanishing quark
267 masses. In this limit quarks are either left or right handed, such that the QCD Lagrangian
268 is symmetric. However, when quarks are confined inside hadrons they have large dynamical
269 masses, called constituent or QCD masses. Here the chiral symmetry is said to be "broken"
270 (or hidden). In the small "s limit some quarks will have small mass, called current mass.
271 In this limit, chiral symmetry is said to be (partially) restored. In our world, quarks and
272 gluons are confined inside hadrons. By significantly increasing the temperature and energy
273 density the strong force holding the quarks and gluons together may be reduced, unbinding
274 them from the hadrons. This phenomenon is known as "de-confinement". De-confinement
275 implies that there exists a phase transition from a gas of hadrons to a new form of matter
276 of free quarks and gluons, called the Quark-Gluon Plasma (QGP).

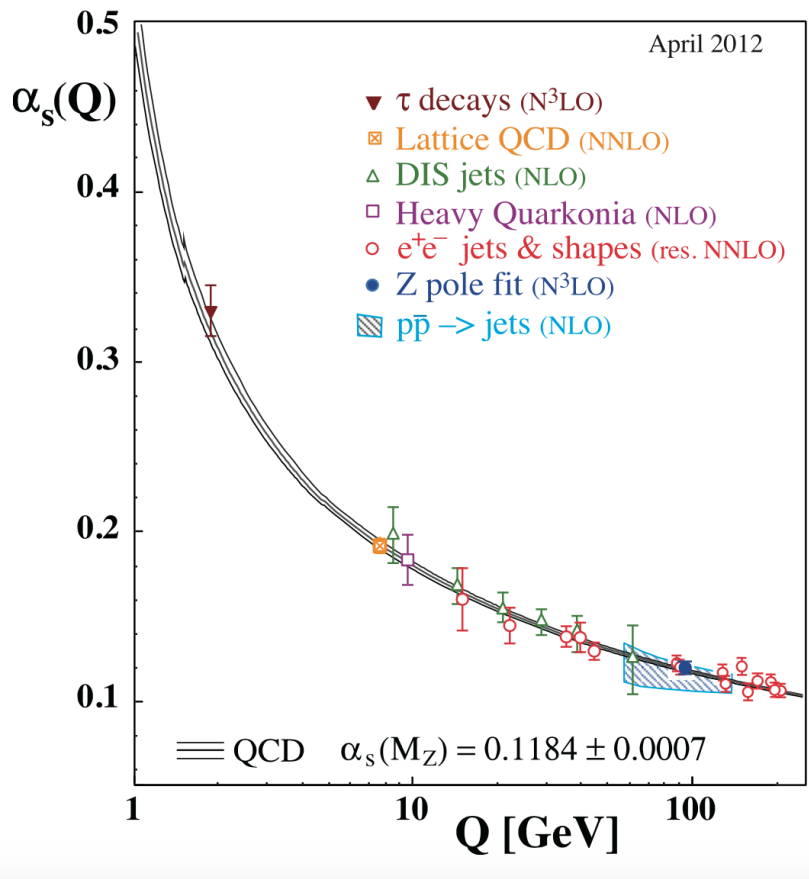


Figure 2: Summary of measurements of α_s as a function of the respective energy scale Q . The respective degree of QCD perturbation theory used in the extraction of α_s is indicated in brackets (NLO: next-to-leading order; NNLO: next-to-next-to leading order; res. NNLO: NNLO matched with resummed next-to-leading logs; N3LO: next-to-NNLO) [1]

277 **1.3 Heavy Ion Collisions**

278 In the case a QGP is formed, it will eventually expand because of its internal pressure.
279 As the system expands it also cools. The space-time evolution of the expansion can be
280 seen in Figure 3 (right side). A and B represent the two incoming ion beams. After a pre-
281 equilibrium phase a QGP is formed. As it expands, the system will eventually reach what
282 is known as the critical temperature (T_c). At this point partons begin to hadronize and this
283 will continue until the chemical freeze-out (T_{ch}) takes place, when inelastic collisions cease.
284 At this stage the distribution of hadrons is frozen. As cooling and expansion continue the
285 hadrons reach what is called thermal freeze out (T_{fo}). Here the elastic collisions stop and
286 the hadrons carry fixed momenta. The QGP state can not be directly observed, because of
287 its short lifetime. Instead, through experiment we measure the final state hadrons, which
288 have a fixed momentum after T_{fo} . The observables of interest should tell us about the
289 de-confinement and the thermodynamic properties of the matter. Moreover, experimental
290 measurements include yields and p_T spectra of various particle species, azimuthal studies
291 of high p_T particles, phase space distributions, and particle correlations.

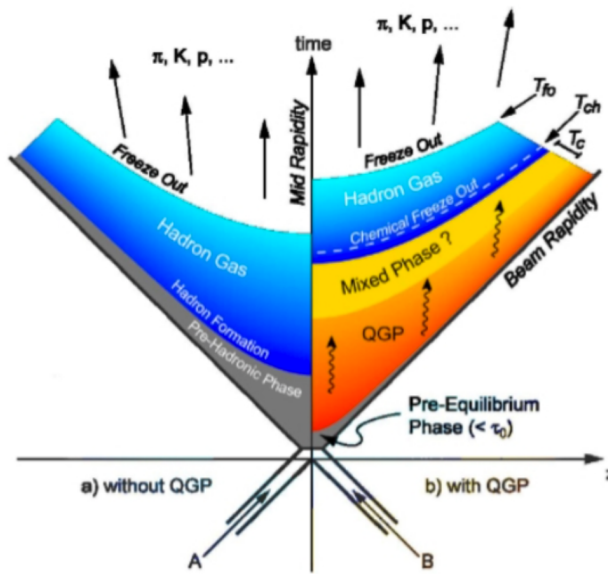


Figure 3: Hydrodynamic evolution of a heavy ion collision with and without the formation of a QGP.

292 **2 Production of resonance with strangeness**

293 **2.1 Resonance with strangeness**

294 **3 Theoretical models**

295 **3.1 Thermal statistical model**

296 The statistical-thermal model has proved extremely successful in applications to relativistic
297 collisions of both heavy ions and elementary particles. In light of this success, THERMUS,
298 a thermal model analysis package, has been developed for incorporation into the object-
299 oriented ROOT framework [13].

300
301 There are three types of statistical-thermal models in explaining data in high energy nu-
302 clear physics and THERMUS treats the system quantum numbers B (baryon number), S
303 (strangeness) and Q (charge) within three distinct formalisms:

304 1. **Grand-Canonical Ensemble:** Because the hot dense matter produced in nucleus-
305 nucleus collisions is large enough, this ensemble is the most widely used in applications
306 to heavy-ion collisions, in which the quantum numbers are conserved on average.

307 2. **Fully-Canonical Ensemble:** In which B, S and Q are each exactly conserved and
308 this ensemble used in high-energy elementary collisions such as pp, p \bar{p} and e $^-$ e $^+$
309 collisions.

310 3. **Strangeness-Canonical Ensemble:** In small systems or at low temperatures, a
311 canonical treatment leads to a suppression of hadrons carrying non-zero quantum
312 numbers, since these particles have to be created in pairs and the resulting low
313 production of strange particles requires a canonical treatment of strangeness.

314 In order to calculate the thermal properties of a system, one starts with an evaluation
315 of its partition function. The form of the partition function obviously depends on the
316 choice of ensemble. In the present analysis the strangeness-canonical ensemble used and
317 the statistical-thermal model requires six parameters as input: the chemical freeze-out
318 temperature T , baryon and charge chemical potentials μ_B and μ_Q respectively, canonical
319 or correlation radius, R_C ; the radius inside which strangeness is exactly conserved and the
320 fireball radius R . An additional strangeness saturation factor γ_S has been used as indicator
321 of a possible departure from equilibrium and $\gamma_S = 1.0$ corresponds to complete strangeness
322 equilibration.

323 The volume dependence cancels out when studying the particle ratios as well as strangeness
324 canonical equivalent to grand canonical formalism if $\Delta S = 0$ in the ratios and γ_S also can-
325 celes out. Parameters used in the analysis listed in Table 1. The μ_B parameter taken from
326 the Ref. [14].

Table 1: Parameters used in the thermal-model calculations.

Parameter	Value
T (MeV)	varied (see text)
μ_B (MeV)	$9.2 \times 10^{-2}????$
μ_Q (MeV)	0.0
γ_S	1.0

328 **3.1.1 Calculations**

329 *Concept:*

330 In order to calculate the particle ratios within strangeness canonical formalism of THER-
 331 MUS, temperature varied between 60 MeV to 180 MeV and particle yields extracted for
 332 each temperature value and then primary particle ratios calculated for each case.

333

334 *Feed-Down Correction:*

335 Since the particle yields measured by the detectors in collision experiments include feed-
 336 down from heavier hadrons and hadronic resonances, the primordial hadrons are allowed to
 337 decay to particles considered stable by the experiment before model predictions are com-
 338 compared with experimental data. In the analysis only Λ particles counted as stable (do not
 339 allowed to decay) so there is no feed-down contribution from these particles to the other
 340 ratios.

341

342

343 Properties of studied particles and their particle ratios listed in Table 2 and Table 3,
 344 respectively.

Table 2: Properties of particles used in the ratio calculations.

Particle	Δ^{++}	p	K^{*0}	K^0	K^+	Λ^*	Λ	Σ^{*+}	Σ^+	Σ^0
Mass (MeV/c^2)	1232	938.27	895.92	497.61	493.67	1519.5	1115.68	1382.8	1189.37	1192.6
Width (MeV/c^2)	120	–	50.7	–	–	15.6	–	37.6	–	–
$c\tau$ (fm)	1.6	–	3.9	–	–	12.6	–	5.51	–	–
Ang. Momentum (J)	3/2	1/2	1	1	0	3/2	1/2	3/2	1/2	1/2
Isospin (I)	3/2	1/2	1/2	1/2	1/2	0	0	1	1	1
Parity (P)	+1	+1	-1	-1	0	-1	+1	+1	+1	+1
Strangeness (S)	0	0	1	1	1	-1	-1	-1	-1	-1
Baryon Number (B)	1	1	0	0	0	1	1	1	1	1
Decay Channel	$p\pi^+$	–	π^-	–	$\mu^+\nu_\mu$	pK^-	$p\pi^-$	$\Lambda\pi^+$	$p\pi^0$	$\Lambda\gamma$
Branching Ratio (%)	~ 100	–	~ 66.7	–	~ 63.54	~ 45	~ 63.9	~ 87	~ 51.6	~ 100
Q-Value(MeV/c^2)	154.16	–	262.68	–	–	87.55	37.84	127.55	111.53	76.96

345

346

347 **3.1.2 Results**

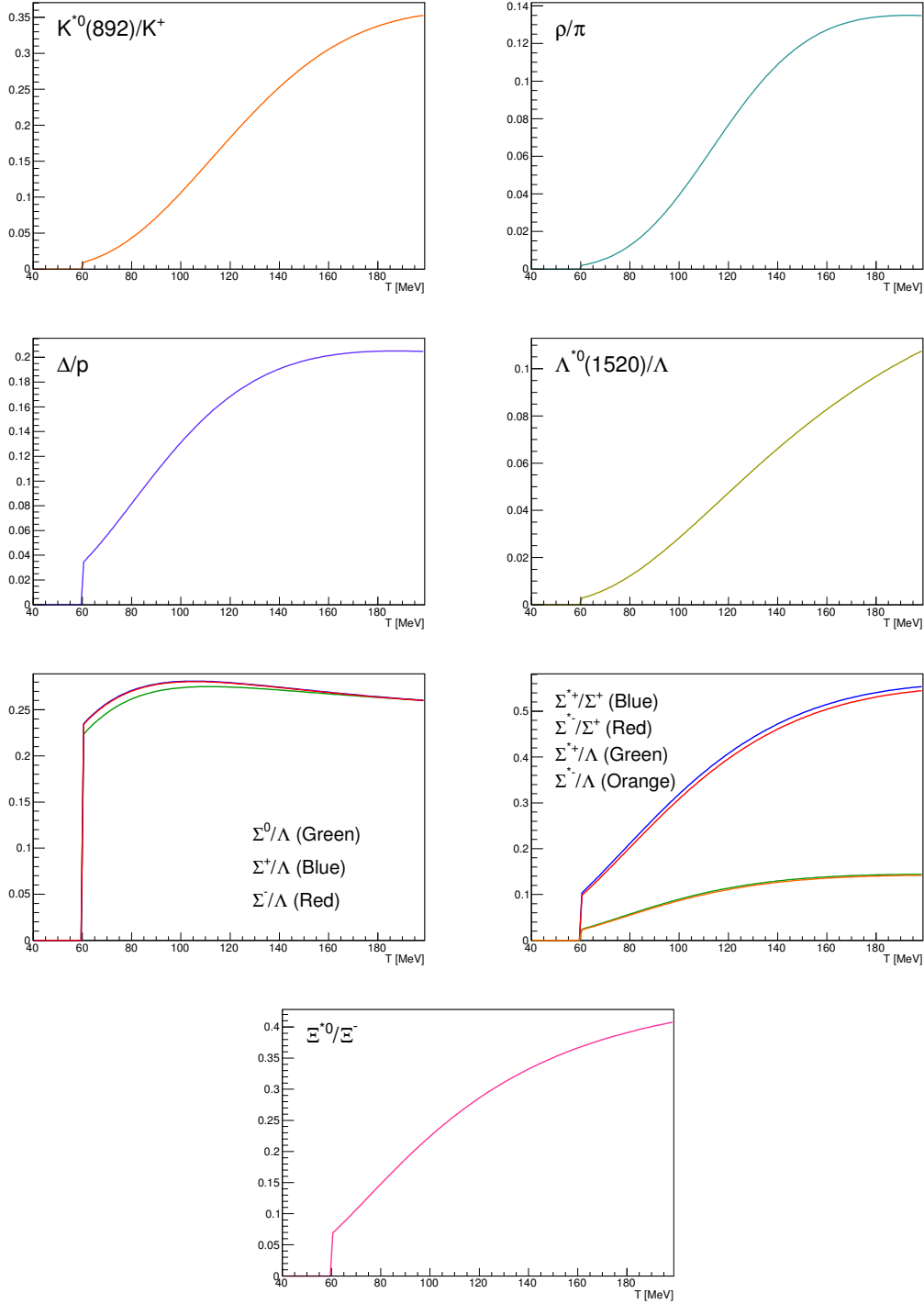


Figure 4: Ratio of baryonic and mesonic resonances over their stable partner as a function of temperature.

Table 3: Difference of mass (ΔM), baryon number (ΔB), strangeness (ΔS) and charge (ΔQ) of the ratios. The values of the slopes needs to be checked!!!!

Particle	Δ^{++}/p	K^*/K^+	Λ^*/Λ	Σ^{*+}/Λ	Σ^{*+}/Σ^0	Σ^0/Λ	Σ^{*+}/Σ^+	Ξ^{*0}/Ξ^-
ΔM (MeV/ c^2)	293.8	402.25	403.82	267.12	190.16	76.96	193.43	210.49
ΔB	0	0	0	0	0	0	0	0
ΔS	0	0	0	0	0	0	0	0
ΔQ	+1	-1	0	+1	0	+1	0	-1
Slope (%) per MeV ????????	0.19	0.76	0.98	0.25	-	-0.08	0.37	0.42

348 3.1.3 Comparison with data

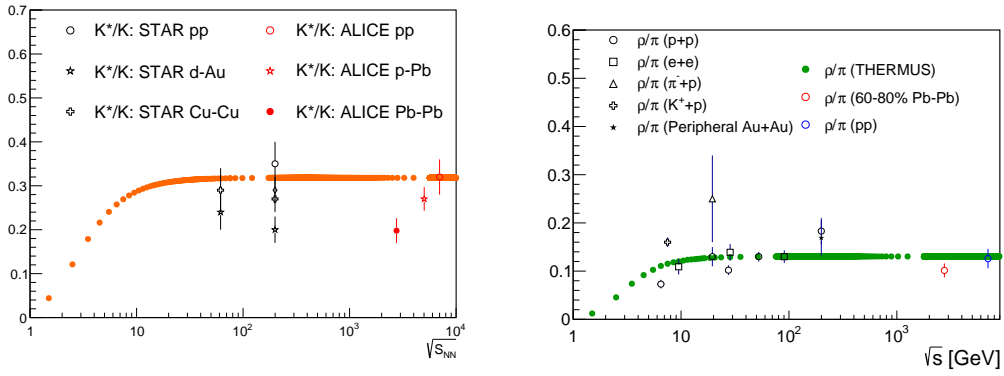


Figure 5: Ratio of resonances over their stable partner as a function of $\sqrt{(s)}$.

349 3.2 UrQMD

350 **4 A Large Ion Collider Experiment at the LHC**

351 ALICE (A Large Ion Collider Experiment) has been collecting data during the whole first
352 phase of the Large Hadron Collider operations, from its startup on the 23 November 2009
353 to the beginning of the first long technical shutdown in February 2013. During the first
354 three years of operations LHC provided pp collisions at 0.9, 2.76, 7 and 8 TeV, Pb–Pb colli-
355 sions at 2.76A TeV and finally p–Pb collisions at 5.02 TeV. The first section of this chapter
356 focuses on the LHC performance during this phase and includes details on the accelerator
357 parameters that allow the LHC to perform as a lead ion collider. A detailed description
358 of the ALICE detector follows in the section 4.2.1. ALICE has been designed and op-
359 timized to study the high particle-multiplicity environment of ultra-relativistic heavy-ion
360 collisions and its tracking and particle identification performance in Pb–Pb collisions are
361 discussed. The attention is drawn in particular on the central barrel detectors. Section
362 4.2.2 describes the ALICE Data Acquisition (DAQ) system, that also embeds tools for the
363 online Data Quality Monitoring (DQM). The final part of the chapter is dedicated to the
364 offline computing and reconstruction system based on the GRID framework.

365 **4.1 The Large Hadron Collider**

366 The Large Hadron Collider (LHC) [15] at CERN is the biggest particle accelerator world-
367 wide. The LHC project was approved in 1994 and construction works in the existing
368 underground tunnel started in 2001 after the dismantling of the LEP collider, which had
369 previously been built in the tunnel which is located under the Swiss-French border area
370 close to Geneva at a depth of 50 to 175 m. The LHC has a circumference of 26.7 km. By
371 design, its maximum achievable energies are 7 TeV for beam of protons and 2.76 TeV per
372 nucleon for beam of lead ions, thus providing collisions at $\sqrt{s} = 14$ TeV and $\sqrt{s_{NN}} = 5.5$
373 TeV, respectively. These would be the largest energies ever achieved in particle collision
374 experiments. The LHC is a synchrotron that accelerates two counter-rotating beams in
375 separate parallel beam pipes. In each of them bunches of particles travel many times
376 around the accelerator ring before the collision energy is reached. The accelerator has to
377 bend the beams around the ring, keep the bunches focused and accelerate them to their
378 collision energy. Finally, the spatial dimension of the bunches has to be minimized in order
379 to attain high luminosity, which ensure a high number of collisions per time interval at
380 the collision points, i.e. a high luminosity. A combination of magnetic and electric field
381 components performs the mentioned tasks. Despite the high luminosity reached, only a
382 very small fraction of the particles of two bunches collides in a single bunch crossing. The
383 others leave the interaction region essentially uninfluenced, are defocused, and continue to
384 circulate in the accelerator.

385 Injection of bunches into the LHC (Figure 6) is preceded by acceleration in the LINAC2,
386 PS booster, PS, and SPS accelerators. The acceleration sequence is slightly different for
387 heavy-ions, in which case bunches pass the LINAC3, LEIR, PS, and SPS accelerators

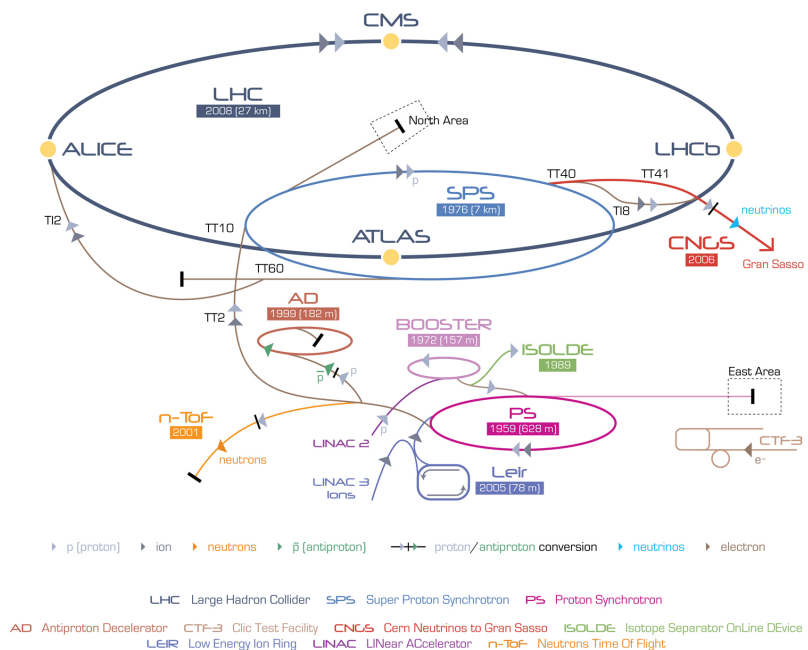


Figure 6: The CERN accelerator complex [2]

(more information can be found in [90]). Several injections to the LHC are needed until all bunches of both beams are filled. The first pp collisions at 900 GeV centre-of-mass energy were delivered by the LHC on September 10th 2008. Nine days later, the operations were interrupted due to a failure in an electrical connection between two magnets. The machine operators spent over a year repairing and consolidating the accelerator. On November 20th 2009 low energy proton beams circulated again, and a few days later, by achieving the energy of 1.18 TeV per proton beam, LHC became the most powerful accelerator in the world. The first pp collisions at centre-of-mass energy of 7 TeV were delivered in March 2010, and the first Pb?Pb collisions at centre-of-mass energy of 2.76 TeV per nucleon pair in November 2010. In 2010 the integrated luminosity delivered by the LHC was $\sim 48 \text{ pb}^{-1}$ for pp collisions at $\sqrt{s} = 7 \text{ TeV}$ ($\sim 0.5 \text{ pb}^{-1}$ in ALICE) and $\sim 10 \mu\text{b}^{-1}$ for Pb?Pb at $\sqrt{s_{\text{NN}}} = 2.76 \text{ TeV}$ ($\sim 10 \mu\text{b}^{-1}$ in ALICE). In 2011 the beam energy was the same as in 2010 both for pp and Pb-Pb. The performance of the LHC improved in terms of luminosity with $\sim 5.61 \text{ fb}^{-1}$ for pp ($\sim 2 \text{ pb}^{-1}$ in ALICE) and $\sim 166 \mu\text{b}^{-1}$ for Pb-Pb collisions ($\sim 143.62 \mu\text{b}^{-1}$ in ALICE). In 2012, the centre-of-mass energy for pp collisions was brought to 8 TeV and the integrated luminosity (up to December 2012, end of the pp program) was $\sim 23.3 \text{ fb}^{-1}$ ($\sim 10 \text{ pb}^{-1}$ in ALICE). A pilot p-Pb run operated at $\sqrt{s_{\text{NN}}} = 5.02 \text{ TeV}$ on September 2012, followed by a long p-Pb run on February 2013 with a delivered luminosity of 31.2 nb^{-1} . A very short pp run at $\sqrt{s} = 2.76 \text{ TeV}$ ended the Run1 of the LHC program, marking the start of the first long shutdown (LS1) until the end of 2014. Despite its excellent performance, the LHC has not yet achieved the nominal parameters (\sqrt{s}, L), that is the main goal for the next ignition of the machine in 2015. The LHC produces collisions in four so called Interaction Points (IPs) in correspondence of which are located six detectors of different dimensions and with different goals, all able to study the products of the interactions. These are:

ALICE (A Large Ion Collider Experiment-IP₂) [16] is a dedicated heavy-ion experiment designed to study strongly-interacting matter at very high energy density. It explores the phase transition to the QGP, its phase diagram, and its properties. Furthermore, ALICE will also study collisions of protons, on one hand as a baseline for heavy-ion measurements and on the other hand it contributes to measurements of identified particles by making use of its excellent particle identification capability and its acceptance at very low transverse momenta.

ATLAS (A Toroidal LHC ApparatuS-IP₁) and CMS (Compact Muon Solenoid - IP₅) [17][18] are general-purpose detectors for pp collisions that are built to cover the widest possible range of physics at the LHC. Specific topics are the search for the Higgs boson and physics beyond the Standard Model, e.g. new heavy particles postulated by supersymmetric extensions (SUSY) of the Standard Model and evidence of extra dimensions.

LHCb (The Large Hadron Collider beauty experiment-IP₈) [19] is a dedicated

429 experiment for the study of heavy flavor physics at the LHC. In particular, the experiment
430 focuses on the study of CP violation and rare decays of beauty and charm particles, to
431 test the Standard Model and to search for evidence of New Physics. The LHCb physics
432 program is complementary to the flavor physics studies conducted at the B-factories and
433 to the direct searches for new particles performed at ATLAS and CMS.

434

435 **LHCf (Large Hadron Collider forward experiment-IP₁)** [20] measures forward
436 particles created during LHC collisions to provide further understanding of high energy
437 cosmic rays. The detector is placed close to the ATLAS experiment.

438

439 **TOTEM (TOTal Elastic and diffractive cross-section Measurement-IP₅)** [21]
440 measures the total cross-section, elastic scattering, and diffractive processes. The detector
441 is located close to the CMS experiment.

442

443 4.2 The ALICE project

444 The ALICE experiment at the LHC [22] has as main goal the study of nuclear matter
445 under extreme conditions of temperature and energy density such as those reached in ultra-
446 relativistic heavy-ion collisions. The aim is to verify the QCD prediction of the existence of
447 a phase transition from the common hadronic matter to the Quark-Gluon Plasma. Since
448 ALICE is the only LHC experiment specifically designed for Pb–Pb collisions, it has to
449 be able to cope with the large multiplicities associated with these collision systems and at
450 the same time has to cover as many QGP-related observables as possible. ALICE is also
451 interested in the study of pp interactions, as these are crucial for a comparison with Pb–Pb
452 collisions, to tune Monte Carlo models and per se, like the other LHC experiments. With
453 respect to these experiments, ALICE is endowed with an excellent Particle IDentification
454 (PID) performance, obtained combining different PID techniques from different detectors
455 that are optimized in different momentum (p) regions.

456 4.2.1 ALICE detector

457 ALICE is a complex of 14 detector subsystems (Figure 7) that can be classified in three
458 groups:

459

460 **Central detectors** are housed in a solenoid magnet which provides the experiment
461 with a 0.5 T magnetic field and covers the pseudo-rapidity interval $-0.9 < \eta < 0.9$ (corre-
462 sponding to a polar acceptance $\pi/4 < \theta < 3\pi/4$). The azimuthal acceptance is 2π . They
463 are mainly dedicated to vertex reconstruction, tracking, particle identification and momen-
464 tum measurement. Starting from the interaction region and going outward, we find the
465 following detectors:

- Inner Tracking System (ITS)
- Time Projection Chamber (TPC)
- Transition Radiation Detector (TRD)
- Time Of Flight (TOF)

470 In the mid-rapidity region there are also three detectors with limited azimuthal accep-
 471 tance:

- High Momentum Particle Identification Detector (HMPID)
- PHOton Spectrometer (POHS)
- ElectroMagnetic CALorimeter (EMCAL)

475 **Muon spectrometer** is placed in the forward pseudo-rapidity region ($-4.0 < \eta < -2.5$) and consists of a dipole magnet and tracking and trigger chambers. It is optimized to
 476 reconstruct heavy quark resonances (such as J/Ψ through their $\mu^+\mu^-$ decay channel) and
 477 single muons.

479 **Forward detectors** are placed in the high pseudo-rapidity region (small angles with
 480 respect to the beam pipe). They are small and specialized detector systems used for
 481 triggering or to measure global event characteristics. They are:

- Time Zero (T0) to measure the event time with precision of the order of tens of picoseconds, as needed by TOF
- VZERO (V0) to reject the beam-gas background and to trigger minimum bias events
- Forward Multiplicity Detector (FMD) to provide multiplicity information over a large fraction of the solid angle ($-3.4 < \eta < -1.7$ and $1.7 < \eta < 5$)
- Photon Multiplicity Detector (PMD) to measure the multiplicity and the spatial distribution of photons on an event-by-event basis in the $2.3 < \eta < 3.7$ region
- Zero Degree Calorimeter (ZDC) to measure and trigger on the impact parameter. The ZDC consists of two calorimeters, one for neutrons (ZDC:ZN) and one for protons (ZDC:ZP), and includes also an electromagnetic calorimeter (ZEM)

493 The ALICE global coordinate system [23] is a right-handed orthogonal Cartesian system
 494 with the origin X, Y, Z = 0 at the centre of the detector. The three Cartesian axes are
 495 defined as follows: the X axis pointing towards the centre of the LHC, the Y axis pointing
 496 upward and the Z axis parallel to the local mean beam line pointing in the direction opposite

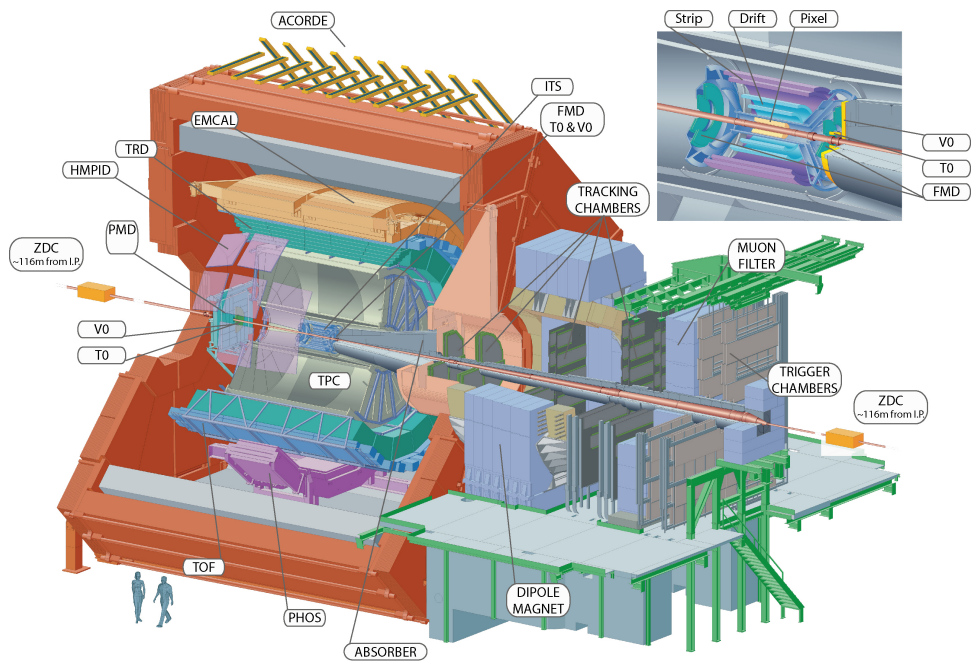


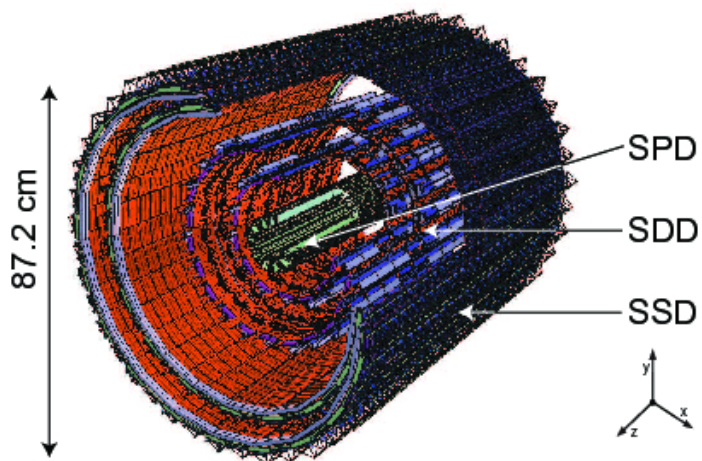
Figure 7: The ALICE detector

497 to the muon spectrometer. The azimuthal angle increases counter-clockwise from the
498 positive X axis ($\Phi = 0$) to the positive Y axis ($\Phi = \pi/2$) with the observer standing at
499 positive Z and looking at negative Z; the polar angle increases from the positive Z axis (θ
500 = 0) to the X-Y plane ($\theta = \pi/2$) and to the negative Z axis ($\theta = \pi$).

501 In the following Sections more specific descriptions of the detectors used in the identifi-
502 cation of the $\Xi(1530)^0$ baryons and in the determination of the characteristics of typical
503 collisions will be given.

504 **ITS**

505 The ITS [22] (Figure 8) is the barrel detector closest to the beam pipe. Its main goals are:



507 Figure 8: Schematic view of the ITS [3]

- 508 • to contribute with the TPC to the global tracking of ALICE by improving the angle
509 and momentum resolution
- 510 • to reconstruct the position of the primary interaction vertex
- 511 • to reconstruct secondary vertices from decays of heavy-flavor and strange particle
512 decays;
- 513 • to track and identify particles with momentum below $100 \text{ MeV}/c^2$
- 514 • to improve the momentum, impact parameter and angle resolution for the measure-
515 ment of high p_T particles performed with the TPC

- 516 • to reconstruct particles traversing dead regions of the TPC

517 The ITS surrounds the beam pipe (which is a 800 μm thick cylinder with an outer
 518 diameter of 2.9 cm) and consists of six cylindrical layers of silicon detectors located at radii
 519 between 4 cm and 43 cm. Due to the high track density, the two innermost layers are
 520 Silicon Pixel Detectors (SPD) which guarantee a high granularity. They are followed by
 521 two layers of Silicon Drift Detectors (SDD), while the two outmost layers are double-sided
 522 Silicon micro-Strip Detectors (SSD).

523 Since the momentum and impact parameter resolutions for low momentum particles
 524 are dominated by multiple scattering effects, the amount of material in the active volume
 525 has been minimized as much as possible. The granularity of the detector was optimized to
 526 keep the occupancy low in all the layers. With the technology chosen, the ITS detectors
 527 reach a spatial resolution of the order of a few tens of m resulting in a resolution on the
 528 impact-parameter⁵ better than 70 m in the r plane for $p_T > 1 \text{ GeV}/c$ and thus well suited
 529 for the reconstruction of heavy-flavor decays (see Figure 9).

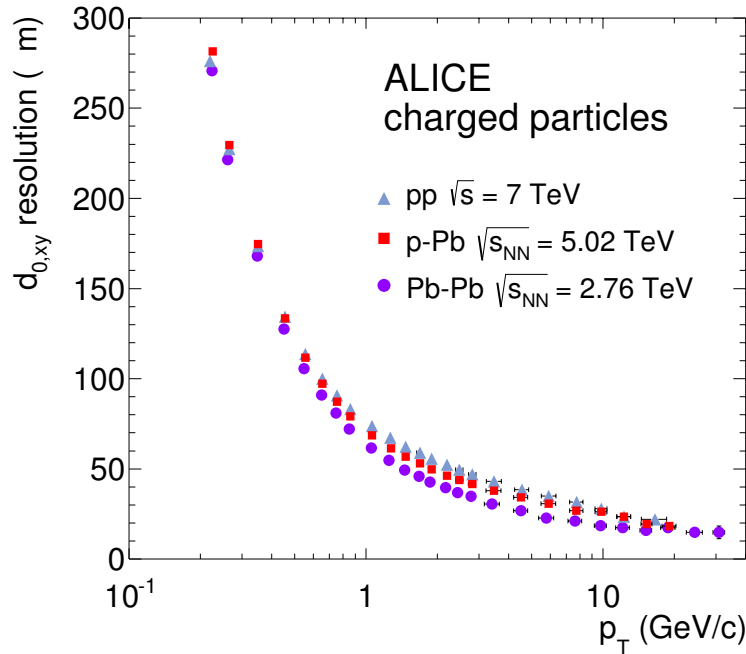


Figure 9: Track impact parameter resolution in the transverse plane ($r\phi$) vs p_T for charged particle

530 **TPC**

531 The TPC [24] (Figure 10) is the main tracking detector of the central barrel, optimized

532 to provide, together with the other central barrel detectors, charged- particle momentum
 533 measurements with good two-track separation, particle identification and vertex determina-
 534 tion. The TPC was designed for an excellent tracking performance in the high multiplicity
 535 environment of Pb–Pb collisions. For this reason, it was chosen to be a drift chamber,
 536 cylindrical in shape, 5 m long, with the inner radius ($r_{in} \sim 85$ cm) determined by the
 537 maximum acceptable track density, and the external one ($r_{ext} \sim 250$ cm) by the minimum
 538 track length for which dE/dx resolution is $< 10\%$. The TPC volume is filled with 90 m^3 of
 539 Ne/CO₂/N₂ (90/10/5). The readout planes are divided in 18 sectors in which multi-wire
 540 proportional chambers (with cathode pad readout) are housed. Because of its good dE/dx
 541 resolution, the TPC can identify particles with $p_T < 1\text{ GeV}/c$ on a track-by-track basis.

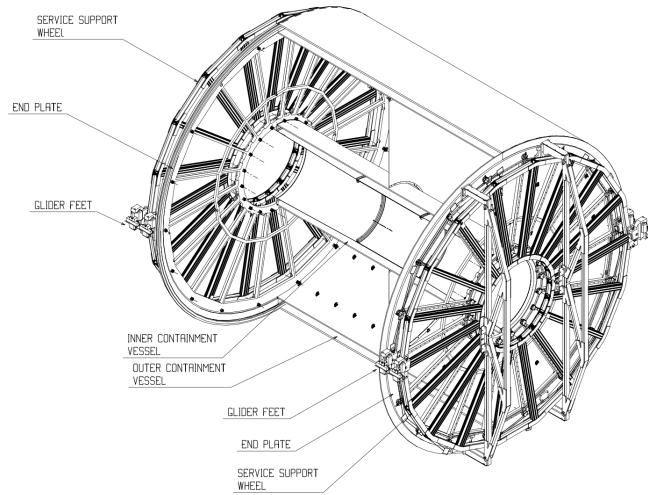


Figure 10: Schematic view of the TPC

542 Charged particles traveling through the TPC ionize the detector's gas; the measure-
 543 ment of this loss of energy is what we need to identify a particle. The physics observable
 544 in this case is the energy loss per unit length, within the matter crossed by the charged
 545 particle, which we call specific energy loss, also denoted by dE/dx . This is described by
 546 the Bethe–Bloch equation, 8, that highlights the key of the identification technique: this
 547 observable depends only on the charge and on velocity (β) of the particle, which, in turn,
 548 depends only on the momentum and the mass of the ionizing particle. Since momentum is
 549 already known due to track curvature and charge is unitary for most measured tracks, mea-
 550 suring the dE/dx allows us to indirectly determine mass and thus determine the particle
 551 species. The Bethe-Bloch equation gives the mean specific energy loss:

$$-\langle \frac{dE}{dx} \rangle = k_1 \cdot z^2 \frac{Z}{A} \cdot \frac{1}{\beta^2} \left[\frac{1}{2} \ln(k_2 \cdot m_e c^2 \cdot \beta^2 \gamma^2) - \beta^2 + k_3 \right] \quad (8)$$

552 where $\beta\gamma = p/Mc$ and: Z: atomic number of the ionized gas (in this case Ne/CO₂/N₂)
 553 A: mass number of the ionized gas (g/mol)
 554 m_e: electron mass
 555 z: electric charge of the ionizing particle in unit of electron charge e
 556 M: ionizing particle mass
 557 p: ionizing particle momentum
 558 β: ionizing particle velocity normalized to the light velocity c
 559 γ = 1/√(1 - β²), Lorentz factor
 560 k₁, k₂, k₃: constants depending on the ionized medium

561
 562 For a given ionizing particle mass hypothesis, a given momentum and a given length
 563 of the trajectory in the ionizing medium, the total charge deposited along the trajectory
 564 is subject to statistical fluctuations. This random variable follows a Landau distribution,
 565 that give us the opportunity to measure the mean value hdE/dx . The long tail of the
 566 Landau distribution is usually truncated at 50%-70% of the collected signal.

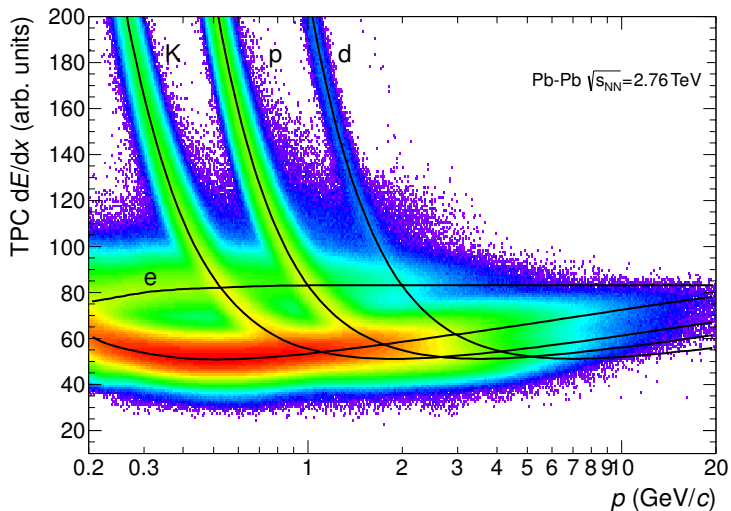


Figure 11: Specific energy loss (dE/dx) in the TPC vs. particle momentum in Pb–Pb collisions at $\sqrt{s_{NN}} = 2.76$ TeV. The lines show the parametrisations of the expected mean energy loss.

567 The specific energy loss in the TPC as a function of momentum is shown in Figure
 568 11. The different bands characteristic for e[±], π[±], K[±], p[±] are clearly visible. These
 569 are the evidence of the statistical distribution of the measured energy loss around the
 570 expected mean value. The expected value correspond to the prediction by a Bethe–Bloch
 571 experimental parametrization (superimposed as black lines in the Figure). For a track

572 within the TPC the relevant quantity to be considered for PID is the difference between
 573 the measured specific energy loss and the corresponding predicted value, by the Bethe-
 574 Bloch parametrization for a given measured momentum. If normalized to the resolution
 575 of the dE/dx measurement in the TPC, this difference could be expressed in number of
 576 σ (see Equation 9). In this way it is possible to estimate more quantitatively the goodness
 577 of a mass hypothesis. This also gives us the possibility to choose the strictness we want to
 578 adopt in the identification of a particle (n_σ , $n = 2, 3, 4$):

$$n_\sigma = \frac{(dE/dx)_{measured} - (dE/dx)_{Bethe-Bloch}}{\sigma_{TPC}} \quad (9)$$

V0

580 The VZERO detector [25] consists of two segmented arrays of plastic scintillator counters,
 581 called VZERO-A and VZERO-C, placed around the beam-pipe on either side of the IP:
 582 one at $Z = 340$ cm, covering the pseudo-rapidity range [2.8; 5.1], and the other at $Z = -90$
 583 cm (in front of the absorber), covering the pseudo-rapidity range [-3.7; -1.7]. They consist
 584 of 32 counters distributed in four rings, each divided in eight 45 sectors. Each counter
 585 is made of scintillator material embedded with WaveLength Shifting fibers. Clear fibers
 586 collect and transport the signal to photomultipliers 3 - 5 m far from the detector, inside
 587 the L3 magnet. The counters have a time resolution better than 1 ns. Their response is
 588 recorded in a time window of 25 ns around the nominal beam crossing time. The VZERO
 589 has an important role in rejecting background from beam-gas collisions (see, Figure 12)
 590 exploiting the relative time-of-flight measurement between the two arrays: when the beam-
 591 gas collision takes place outside the region between the two arrays, particles arrive 6 ns
 592 before or after the time of a beam-beam collision.

593 The VZERO is a trigger detector that will provide a minimum-bias trigger for all
 594 colliding systems to the central barrel detectors and three centrality triggers in p-Pb and
 595 Pb-Pb collisions (multiplicity, central and semi-central).

596 The first parameter to be determined in A-A(p-A) collisions is the centrality(multipliciy).
 597 This is defined according to the value of the impact parameter, b , and provides a geomet-
 598 rical scale of the overlapping region between the colliding nuclei: a collision will be defined
 599 from central to peripheral, as the impact parameter increases. The centrality of a collision
 600 is not directly available and must be deduced from a combination of experimentally mea-
 601 sured quantities and Monte Carlo simulations. There are a number of observables that can
 602 be measured and used as centrality estimators. The charged-particle multiplicity N_{ch} and
 603 the transverse energy E_T measured around mid-rapidity are measurable quantities related
 604 to the energy deposited in the interaction region (these are therefore related to N_{part}).
 605 These variables increase significantly increasing the centrality of the collisions. Another
 606 measurable quantity to estimate the centrality is the zero-degree energy EZDC, namely
 607 the energy carried by spectator nucleons $N_{spec} = 2A - N_{part} = E_{ZDC}/E_A$, where E_A is
 608 the beam energy per nucleon. Typically a measured distribution of one of the previous
 609 observables is mapped to the corresponding distribution obtained from phenomenological

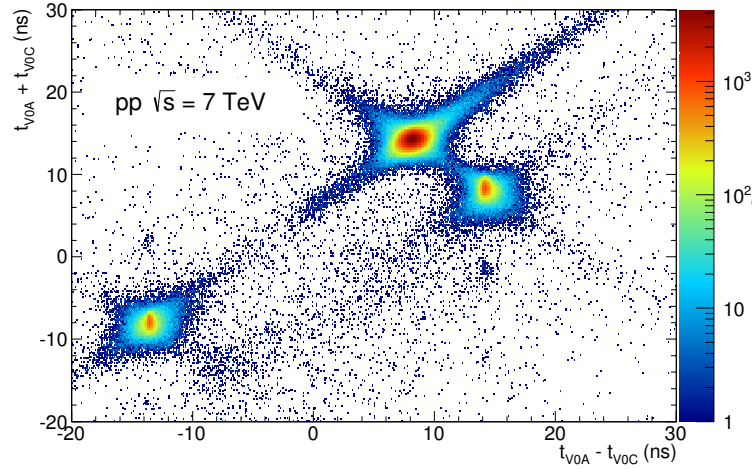


Figure 12: Correlation between the sum and difference of signal times in V0A and V0C. Three classes of events collisions at (8.3 ns, 14.3 ns), background from Beam 1 at (-14.3 ns, -8.3 ns), and background from Beam 2 at (14.3 ns, 8.3 ns) can be clearly distinguished.

610 Glauber calculations. The Glauber model [26, 27] uses a semi-classical approach: the A?A
 611 collision is assumed to be an incoherent superposition of N elementary nucleon- nucleon
 612 collisions. The main parameters of the model are the inelastic nucleon- nucleon collision
 613 cross-section σ_n and the nuclear density distribution $\rho(r)$. In practice, the simulated dis-
 614 tribution well reproduce the measured distribution or the latter is fitted with an analytical
 615 function. The experimental distribution can then be divided in classes with sharp cuts on
 616 the measured observable (E_{ZDC} , E_T or N_{ch}). These "centrality" classes will correspond to
 617 well defined percentage of the integral of the distribution. A given centrality class in the
 618 measured distribution, corresponds to the same class in the simulated distribution, where
 619 the main geometrical variables (N_{part} , N_{coll} and T_{AA}) can be determined. The number of
 620 classes that can be defined depends on the resolution achievable on the selection variable.
 621 In the analysis described in this thesis the centrality(multiplicity) estimation is based on
 622 the measurement of the multiplicities from the VZERO scintillators [28][29]. This is the
 623 method that achieve the best centrality resolution: it ranges from 0.5% in central to 2%
 624 in peripheral collisions. Other methods, as the ones based on the E_{ZDC} measurement or
 625 based on the estimate of the number of tracks in the SPD or TPC, are used to asses a
 626 systematic uncertainty on the centrality determination. The distribution of the VZERO
 627 amplitudes is shown in Figure 13 where the centrality(multiplicity) percentiles are also
 628 indicated.

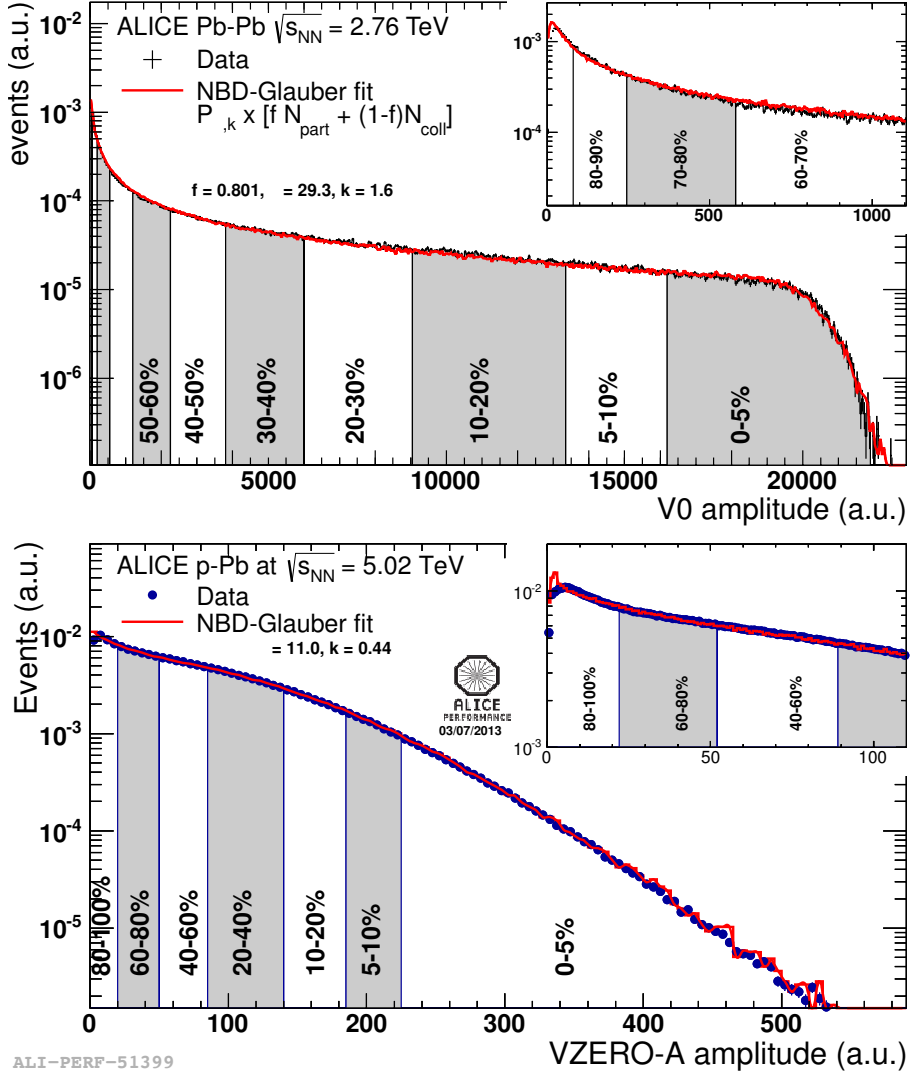


Figure 13: Distribution of the V0 amplitude (sum of V0A and V0C in top, V0A in bottom). The inset shows a magnified version of the most peripheral region.

629 **4.2.2 Data Acquisition (DAQ) and trigger system**

630 The architecture of data acquisition is shown in Figure 14. The tasks of the ALICE DAQ
 631 system are the assembly of event informations from individual detectors into complete
 632 events (event building) as well as buffer- ing and export of assembled events to permanent
 633 storage. The DAQ is designed to process a data rate up to 1.25 GB/s in heavy-ion runs.
 634 Event building is done in two steps. Data from the detectors is received by Detector Data
 635 Links (DDLs) on Local Data Concentrators (LDCs). The LDCs assemble the data into
 636 sub-events that are then shipped to Global Data Collectors (GDCs). A GDC re- ceives all
 637 sub-events from a given event and assembles them into a complete event. These events are
 638 subsequently stored on a system called Transient Data Storage (TDS).

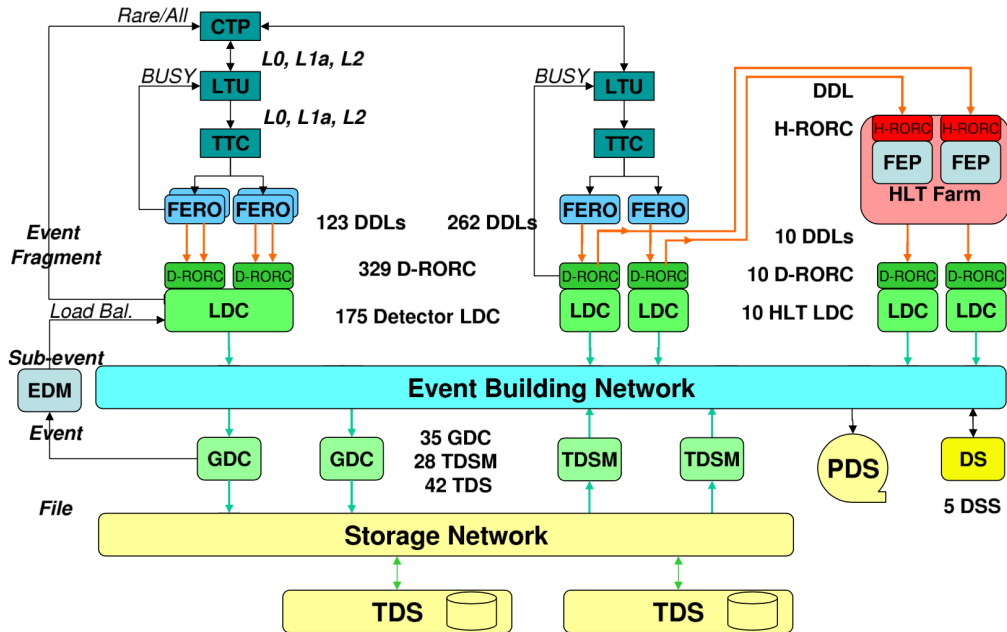


Figure 14: The overall architecture of the ALICE DAQ and the interface to the HLT system.

639 ALICE can simultaneously take data in several partitions, where a set of detec-
 640 tors can store their outputs. Since a partition is a group of commonly controlled detectors, a
 641 given detector can only be active in one partition at a time. The ac-
 642 tive detectors in a given partition may be assigned to data taking groups called clusters, for which triggers

can be defined. Therefore, upon a trigger only a sub-set of the whole partition may be read out. Furthermore, a triggering detector does not have to be necessarily part of the partition. ALICE has a two-layer trigger architecture [30]. The low-level trigger is a hardware trigger called Central Trigger Processor (CTP). The High-Level Trigger (HLT) is implemented as a pure software trigger. The CTP combines inputs from different trigger sources, namely the various detectors. These inputs are single signals, like a hit in the detector, or, can be the result of fast calculation performed directly in the detectors. The HLT allows the implementation of sophisticated logic for the triggering. In contrast to the CTP which governs the readout of the detectors, the HLT receives a copy of the data read out from the detectors and processes them. The hardware trigger combines the trigger signals of the various detectors to decide if an event is accepted, that means it is read out and written to disk. Several trigger levels reduce the event rate depending on the input signals. The first level, called L0, is delivered after 1.2 ?s, while the second, called L1, after 6.5 ?s. The final trigger, L2, is delivered after 100 ?s, upon completion of the drift time in the TPC. Only after an L2 trigger the event is finally stored. The rates of different trigger classes are very different. By definition minimum-bias triggers have the highest rate; other triggers that look for rare signals are characterized by much lower rates. In order to cope with different scenarios, downscaling factors can be applied to the trigger classes individually, i.e. only every nth event fulfilling the trigger condition is read out. The total recording rate is limited by the maximum bandwidth of data that can be recorded to disk and tape. The ALICE software trigger, called HLT, is a farm of multiprocessor computers. The aim is to have about 1000 PCs processing the data in parallel allowing an online analysis of the events. A trigger decision comes from the analysis of a more comprehensive set of information than what happens for the hardware trigger, giving the possibility to apply more sophisticated triggers. Examples include triggers on high energy jets or on muon pairs. Furthermore, the HLT can significantly reduce the event size by selecting regions of interest (partial readout of detectors) and by further compression of the data. The HLT receives a copy of the raw data and performs per detector reconstruction, partly aided by hardware coprocessors. Subsequently, the trigger decision is based on the global reconstructed event. In the same step a region of interest can be selected. In the last optional step, if the trigger decision is positive, the data are compressed. The trigger decision, partial readout information, compressed data, and the re-construction output is sent to LDCs and subsequently processed by the DAQ. In terms of the overall DAQ architecture, data sent by HLT is treated like stemming from a detector.

677 **4.2.3 ALICE offline software frame work**

678 The required computing resources for the reconstruction and analysis of the raw data as
679 well as the production of simulated events needed for the understanding of the data exceed
680 the computing power of single institutes and even centers like CERN. Therefore, institutes
681 that are part of the Collaboration also provide storage and computing resources. Distribu-
682 tion of the data for reconstruction and analysis cannot be performed manually and this
683 led to the need for an automated system. The concept of a decentralized computing model
684 called Grid [31] was identified as a solution.

685

686 *The AliEn Framework*

687 The Grid paradigm implies the unification of resources of distributed computing center,
688 in particular computing power and storage, to provide them to users all over the World.
689 It allows computing center to offer their resources to a wider community and the local re-
690 sources to be shared by an entire collaboration. Software that implements the Grid concept
691 is called Grid middleware. ALICE has developed a Grid middleware called AliEn [32] since
692 2001. An ALICE user employs AliEn to connect to the ALICE Grid which is composed
693 of a combination of general services that are provided by many Grid middleware solutions
694 and ALICE-specific services provided by AliEn. Parts of the ALICE Grid are: i) a global
695 file catalog that is a directory of files in storage elements distributed over the Globe, ii)
696 the automatic matching of jobs for execution to a suitable location in one of the connected
697 sites, iii) a shell-like user interface and iv) API9 services for the ROOT framework [33].

698

699 *AliRoot Framework*

700 AliRoot [22] is the offline framework for simulation, alignment, calibration, reconstruction,
701 visualization, quality assurance, and analysis of experimental and simulated data. It is
702 based on the ROOT framework. Most of the code is written in C++ with some parts in
703 Fortran that are wrapped inside C++ code. Re-usability and modularity are the basic
704 features of the AliRoot framework. Modularity allows parts of the code to be replaced,
705 with minimum or no impact on the rest (for example changing the event generator, the
706 transport Monte Carlo or the reconstruction algorithms). This is achieved implementing
707 abstract interfaces. In addition codes for each detector subsystem are independent modules
708 with their specific code for simulation and reconstruction and the code can be developed
709 concurrently with minimum interference. Re-usability is meant to maintain a maximum
710 amount of backward compatibility as the system evolves.

711 The central module of the AliRoot framework is STEER (Figure 15) which provides
712 several common functions such as: steering of program execution for simulation, reconstruc-
713 tion and analysis; general run management, creation and destruction of data structures,
714 initialization and termination of program phases; base classes for simulation, event genera-
715 tion, reconstruction, detectors elements. For event simulation the framework provides the
716 following functionality:

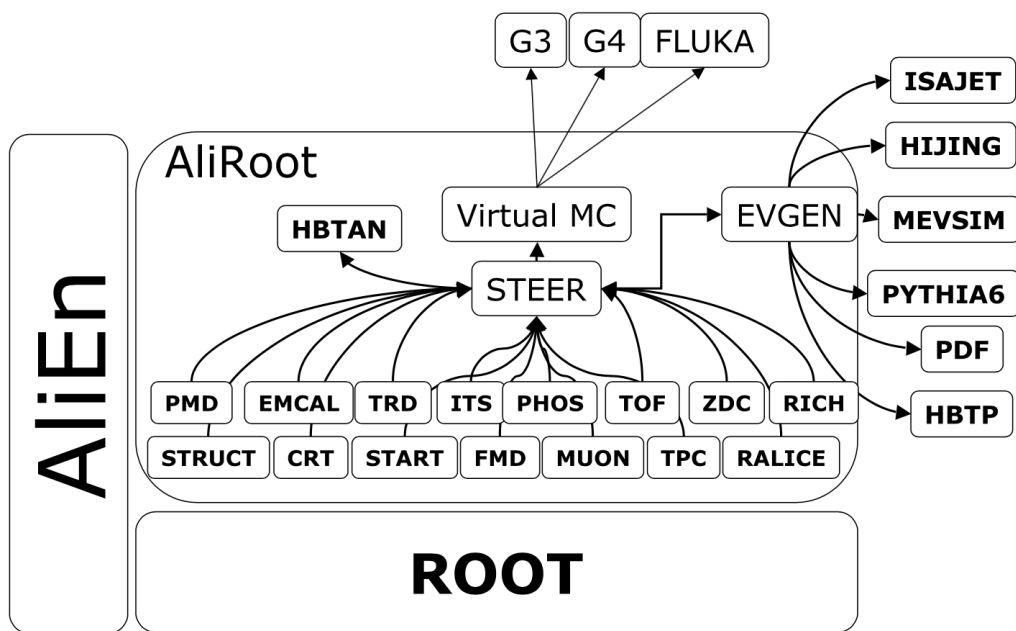


Figure 15: Schematic view of the AliRoot framework

717 **5 Measurement of $\Xi(1530)^0$ production in p–Pb and Pb–Pb**

718 The measurement of resonance production in p–Pb collisions helps to disentangle cold
719 nuclear matter effects from genuine hot medium effects and contribute to the study of
720 the system size dependence of re-scattering in the hadronic phase. And the measurement
721 in ultra-relativistic heavy-ion collisions such as Pb–Pb collisions, provide information on
722 the properties of hadronic medium and different stage of its evolution. In order to study
723 the particle production mechanism in the hadronic phase between the chemical and ki-
724 netic freeze-out, the $\Xi(1530)^0$ resonance production at mid-rapidity ($-0.5 < y_{\text{CMS}} < 0$) is
725 measured in p–Pb collisions $\sqrt{s_{\text{NN}}} = 5.02$ TeV and in Pb–Pb collisions with $|y| < 0.5$ at
726 $\sqrt{s_{\text{NN}}} = 2.76$ TeV with the ALICE experiment, via the reconstruction of its hadronic decay
727 into $\Xi\pi$.

728 **5.1 $\Xi(1530)^0$ -reconstruction**

729 The Ξ^{*0} production in p–Pb and Pb–Pb collisions at mid-rapidity has been studied in dif-
730 ferent multiplicity classes, from very central to peripheral collisions. The analysis strategy
731 is based on the invariant mass study of the reconstructed pairs (referred to as the candi-
732 dates) whose provenance could be the decay of a Ξ^{*0} baryon into charged particles. The
733 decay products (also called daughters in the text) are identified as oppositely charged Ξ and
734 π among the tracks reconstructed in the central barrel. The event selection, track selec-
735 tion and the particle identification strategy is described. The raw signal yield is extracted
736 by fitting the background-subtracted invariant mass distribution in several transverse mo-
737 mentum intervals. In order to extract the p_{T} -dependent cross section, these yields are
738 corrected for efficiency. The p_{T} -dependent correction due to the detector acceptance and
739 reconstruction efficiency, $(\text{Acc} \times \epsilon_{\text{rec}})(\text{pt})$, is computed from a Monte Carlo simulation.
740 The absolute normalisation is then performed, by dividing for the number of the events in
741 each multiplicity and centrality classes.

742 **5.1.1 Data sample and event selection**

743 A description of the ALICE detector and of its performance during the LHC Run 1 (2010–
744 2013) can be found in [22, 34]. The data sample in the analysis from Pb–Pb collisions with
745 energy of $\sqrt{s_{\text{NN}}} = 2.76$ obtained during 2011 and the sample of p–Pb run at $\sqrt{s_{\text{NN}}} = 5.02$
746 TeV was recorded in 2013.

747 Due to the asymmetric energies of the proton (4 TeV) and lead ion (1.57 A TeV) beams,
748 the centre-of-mass system in the nucleon-nucleon frame is shifted in rapidity by $\Delta y_{\text{NN}} =$
749 0.465 towards the direction of the proton beam with respect to the laboratory frame of
750 the ALICE detector [5]. For the analysed p–Pb data set, the direction of the proton beam
751 was towards the ALICE muon spectrometer, the so-called “C” side, standing for negative
752 rapidities; conversely, the Pb beam circulated towards positive rapidities, labelled as “A”

753 side in the following. The analysis in this paper was carried out at midrapidity, in the
754 rapidity window $-0.5 < y_{\text{CMS}} < 0$.

755 The minimum-bias trigger during the p–Pb run was configured to select events by
756 requiring a logical OR of signals in V0A and V0C [34], two arrays of 32 scintillator detectors
757 covering the full azimuthal angle in the pseudo-rapidity regions $2.8 < \eta_{\text{lab}} < 5.1$ and
758 $-3.7 < \eta_{\text{lab}} < -1.7$, respectively [35]. In the data analysis it was required to have a
759 coincidence of signals in both V0A and V0C in order to reduce the contamination from
760 single-diffractive and electromagnetic interactions. Out of this sample in p–Pb collision
761 events about 109.3 million events, 93.9 million events satisfy the following selection criteria
762 and have been actually used for the analysis.

763 The Pb–Pb collisions data sample was selected by online centrality trigger requiring a
764 signal in the forward V0 detectors[29] to record enhanced data in central collision. The
765 data consists of 24.8 million events in most central collisions (0-10%), 21.8 million events in
766 semi-central collisions (10-50%) and 3.5 million events with minimum-bas trigger (0-90%).
767 Among 49.6 million events in total, 43.0 million events have been analyzed as passed the
768 criteria below.

- 769 • Events with z-coordinate of primary vertex (V_z) falling within ± 10 cm from the
770 interaction point
- 771 • Rejection of pile-up event
- 772 • Requiring primary tracks to have at least one hit in one of the two innermost layers
773 of the ITS (silicon pixel detector, SPD)
- 774 • p–Pb: multiplicity ranges in percentile (V0A): 0-20%, 20-40%, 40-60%, 60-100% and
775 MB(0-100%)
- 776 • Pb–Pb: centrallity classes (V0A and V0C): 0-10%, 10-40%, 40-80% and MB (0-80%)

777 The distribution of the vertex z position of the accepted events in p–Pb collision is
778 reported on left panel in Figure 16 and corresponding figure but obtained from Pb–Pb
779 collisions is shown on right panel in Figure. 16. Events with $|V_z| < 10$ cm have been used
780 to ensure a uniform acceptance in the central pseudo-rapidity region, $|\eta| < 0.8$, where the
781 analysis is performed. This cut reduces the total number of events to 97.5 million events,
782 that is the $\sim 89.2\%$ of the initial sample in p–Pb collisions and 43.04 million events which
783 is $\sim 86.8\%$ of the initial sample in Pb–Pb collisions are survived.

784 Fig. 17 shows the multiplicity distribution of the accepted events in p–Pb collision
785 divided in bins of percentile. The each color on the histogram indicate the multiplicity
786 ranges used in this analysis. Corresponding events for each multiplicity range are in Table
787 4.

788 The distribution of centrality in each trigger used to select the events in Pb–Pb collision
789 is shown in Fig. 18 and the reason why the centrality has step structure is that there are

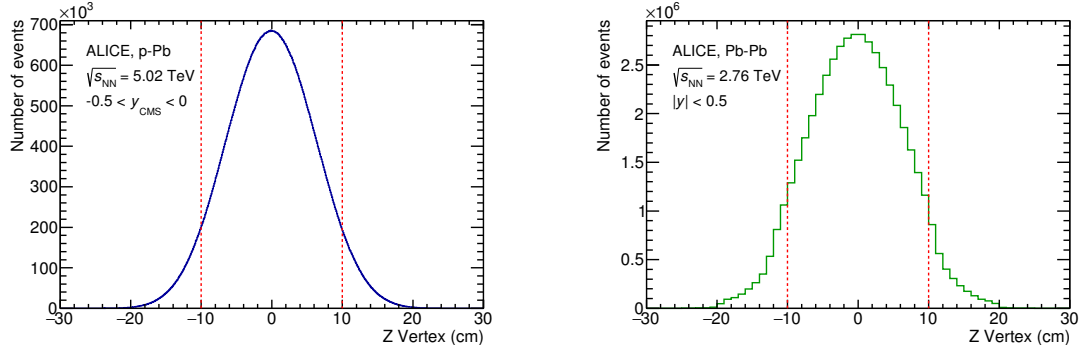


Figure 16: Vertex-z coordinate distribution of the accepted events in p–Pb collision(Left) and in Pb–Pb collisions(Right). The red dashed line indicates vertex cut

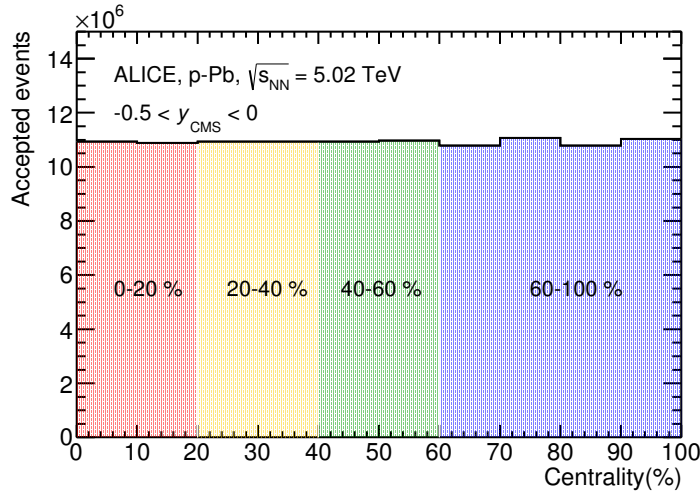


Figure 17: Multiplicity distribution of accepted events in p–Pb collision in percentile. The each color and labels define the four intervals in which the analysis is performed.

790 three different trigger classes classified by the amplitude threshold on VZERO detector.
 791 Because the distribution of events as function of centrality is not a flat, this may lead to
 792 additional bias, in particular when one needs to combine the results from different triggers.
 793 For example, events from 40-80% centrality bin have bias with high statistics in 40-60%. In
 794 order to avoid this effect, we have applied a flattening procedure to have flat distribution
 795 of events as function of centrality. A brief explanation of the method is below :

- 796 1. Histograms are obtained for the effective mass distribution in 1% centrality bins and
 797 for the centrality distribution
- 798 2. The effective mass distributions are scaled in each 1% centrality bin by a factor:
 799 Factor = Nevent in 20-40% / 20 / Nevent in current 1% bin
- 800 3. Each bin in the centrality distribution is scaled using the factor described above
- 801 4. Histograms are added for centrality bins of interest: 0-10%, 10-40%, 40-80%, 0-80%

802 The resulting number of events in each centrality classes is summarized in Table 4.

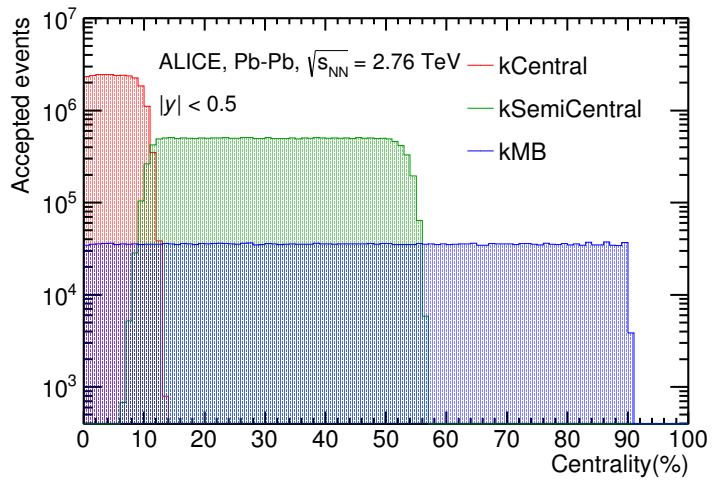


Figure 18: Centrality distribution of three different trigger classes.

p-Pb	0-20%	21.82×10^6
	20-40%	21.86×10^6
	40-60%	21.91×10^6
	60-100%	43.68×10^6
Pb-Pb	0-10%	5.58×10^6
	10-40%	16.73×10^6
	40-80%	22.31×10^6

Table 4: Number of accepted and analyzed events per multiplicity/centrality interval

803 5.1.2 Track and topological selection

804 In comparison with the Ξ^{*0} analysis carried out in pp collisions at $\sqrt{s} = 7$ TeV [7], track
 805 and topological selections were revised and adapted to the p-Pb dataset. Pions from strong
 806 decays of Ξ^{*0} were selected according to the criteria for primary tracks. As summarized
 807 in Table 5, all charged tracks were selected with $p_T > 0.15$ GeV/c and $|\eta_{\text{lab}}| < 0.8$,
 808 as described in Ref. [34]. The primary tracks were chosen with the Distance of Closest
 809 Approach (DCA) to PV of less than 2 cm along the longitudinal direction (DCA_z) and
 810 lower than $7\sigma_r$ in the transverse plane (DCA_r), where σ_r is the resolution of DCA_r . The σ_r
 811 is strongly p_T -dependent and lower than 100 μm for $p_T > 0.5$ GeV/c [34]. To ensure a good
 812 track reconstruction quality, candidate tracks were required to have at least one hit in one
 813 of the two innermost layers (SPD) of the ITS and to have at least 70 reconstructed points in
 814 the Time Projection Chamber (TPC), out of a maximum of 159. The Particle IDentification
 815 (PID) criteria for all decay daughters are based on the requirement that the specific energy
 816 loss (dE/dx) is measured in the TPC within three standard deviations (σ_{TPC}) from the
 expected value (dE/dx_{exp}), computed using a Bethe-Bloch parametrization [34].

Common track selections	$ \eta_{\text{lab}} $	< 0.8
	p_T	> 0.15 GeV/c
	PID $ (\text{d}E/\text{d}x) - (\text{d}E/\text{d}x)_{\text{exp}} $	$< 3 \sigma_{\text{TPC}}$
Primary track selections	DCA_z to PV	< 2 cm
	DCA_r to PV	$< 7\sigma_r$ - $10\sigma_r$ (p_T)
	number of SPD points	≥ 1
	number of TPC points	> 70
	χ^2 per cluster	< 4

Table 5: Track selections common to all decay daughters and primary track selections applied to the charged pions from decays of Ξ^{*0} .

817
 818 Since pions and protons from weak decay of Λ ($c\tau = 7.89$ cm [1]) and pions from weak
 819 decay of Ξ^- ($c\tau = 4.91$ cm [1]) are produced away from the PV, specific topological and

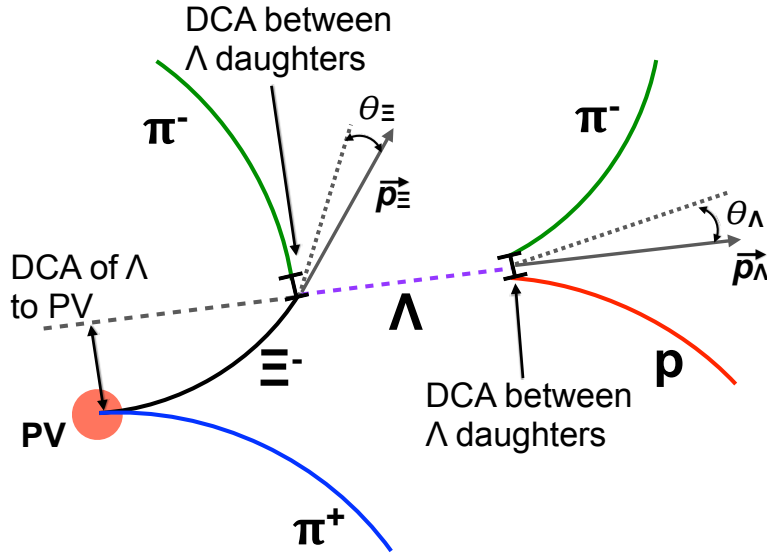


Figure 19: Sketch of the decay modes for Ξ^{*0} and depiction of the track and topological selection criteria.

820 track selection criteria, as summarized in Table 6, were applied [6, 7, 36].

Topological cuts	p-Pb	Pb-Pb
DCA _r of Λ decay products to PV	> 0.06 cm	> 0.11 cm
DCA between Λ decay products	< 1.4 cm	< 0.95 cm
DCA of Λ to PV	> 0.015 cm	> 0.06
$\cos\theta_\Lambda$	> 0.875	> 0.998
$r(\Lambda)$	$0.2 < r(\Lambda) < 100$ cm	$0.2 < r(\Lambda) < 100$ cm
$ M_{p\pi} - m_\Lambda $	$< 7 \text{ MeV}/c^2$	$< 7 \text{ MeV}/c^2$
DCA _r of pion (from Ξ^-) to PV	> 0.015 cm	> 0.035 cm
DCA between Ξ^- decay products	< 1.9 cm	< 0.275
$\cos\theta_\Xi$	> 0.981	> 0.9992
$r(\Xi^-)$	$0.2 < r(\Xi^-) < 100$ cm	$0.2 < r(\Xi^-) < 100$ cm
$ M_{\Lambda\pi} - m_\Xi $	$< 7 \text{ MeV}/c^2$	$< 7 \text{ MeV}/c^2$

Table 6: Topological and track selection criteria.

821 In the analysis of Ξ^{*0} , Λ and π from Ξ^- were selected with a DCA of less than 1.9 cm
 822 and with a DCA_r to the PV greater than 0.015 cm. The Λ daughter particles (π and p)

823 were required to have a DCA_r to the PV greater than 0.06 cm, while the DCA between the
824 two particles was required to be less than 1.4 cm. Cuts on the invariant mass, the cosine
825 of the pointing angle ($\theta_\Lambda, \theta_\Xi$) and the radius of the fiducial volume ($r(\Lambda), r(\Xi)$) in Table 6
826 were applied to optimize the balance of purity and efficiency of each particle sample.

827 **5.1.3 Particle identification**

828 PID selection criteria are applied for

- 829 1. π^\pm (last emitted π) and proton from Λ
830 2. π^\pm (second emitted π) from Ξ^\pm
831 3. π^\pm (first emitted π) from $\Xi(1530)^0$

832 by using TPC. On TPC dE/dx versus momentum distribution, 3σ cuts are applied to TPC
833 for selecting each of the particles. The TPC dE/dx selection allows to have better signal
834 with $\sim 20\%$ increase of significance.

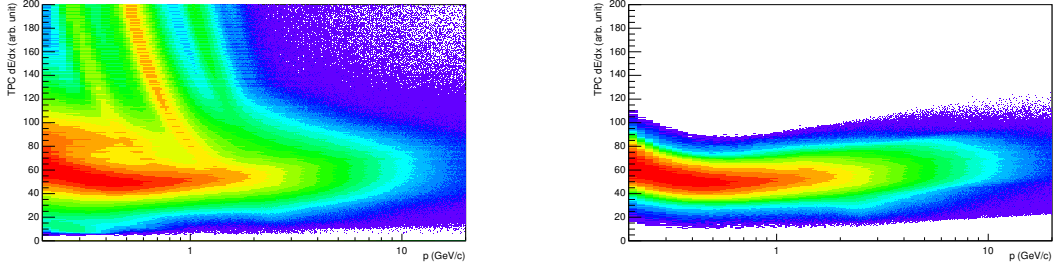


Figure 20: TPC dE/dx as function of transverse momentum for total (top) and selected first emitted π in 3σ (bottom)

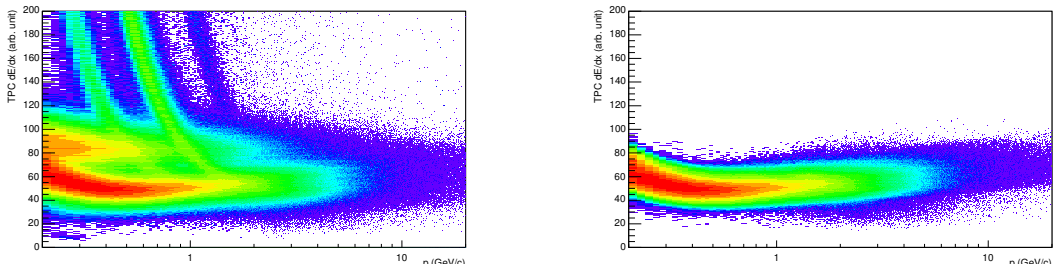


Figure 21: TPC dE/dx as function of transverse momentum for total (top) and selected second emitted π in 3σ (bottom)

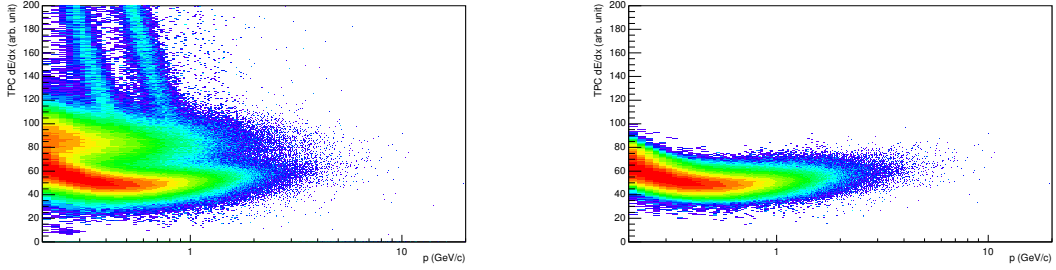


Figure 22: TPC dE/dx as function of transverse momentum for total (top) and selected last emitted π in 3σ (bottom)

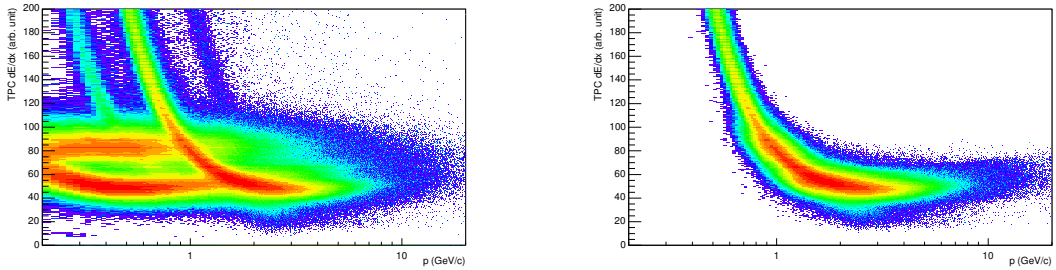


Figure 23: TPC dE/dx as function of transverse momentum for total (top) and selected proton in 3σ (bottom)

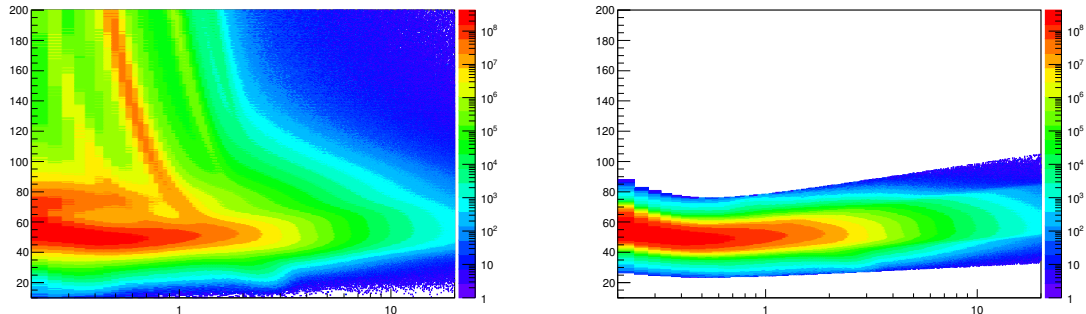


Figure 24: TPC dE/dx as function of transverse momentum for total (top) and selected first emitted π in 3σ (bottom)

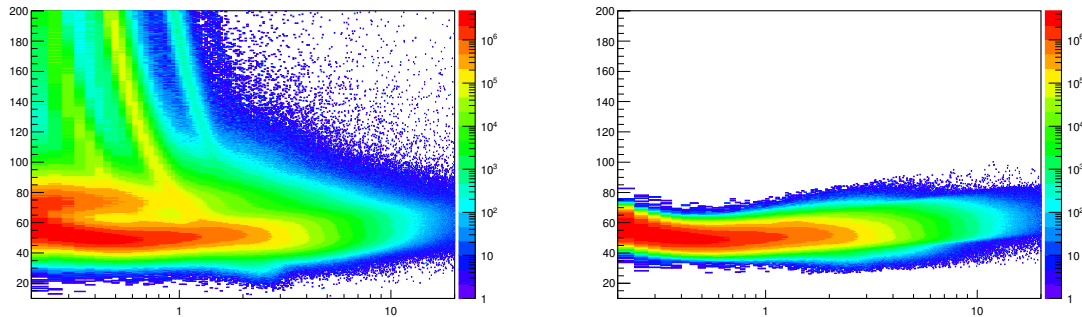


Figure 25: TPC dE/dx as function of transverse momentum for total (top) and selected second emitted π in 3σ (bottom)

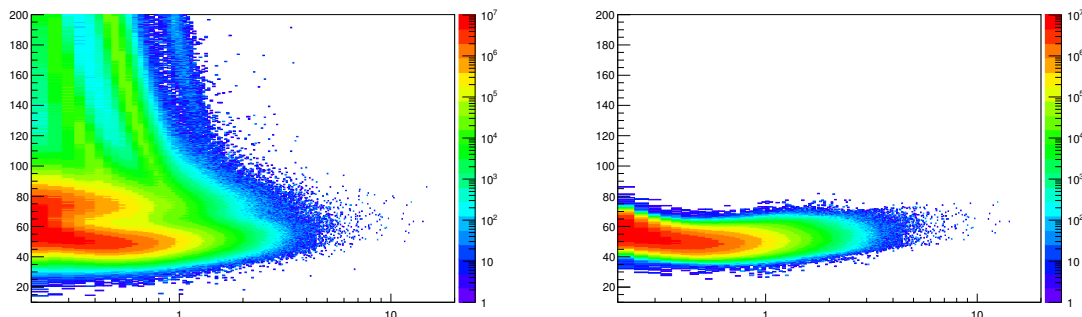


Figure 26: TPC dE/dx as function of transverse momentum for total (top) and selected last emitted π in 3σ (bottom)

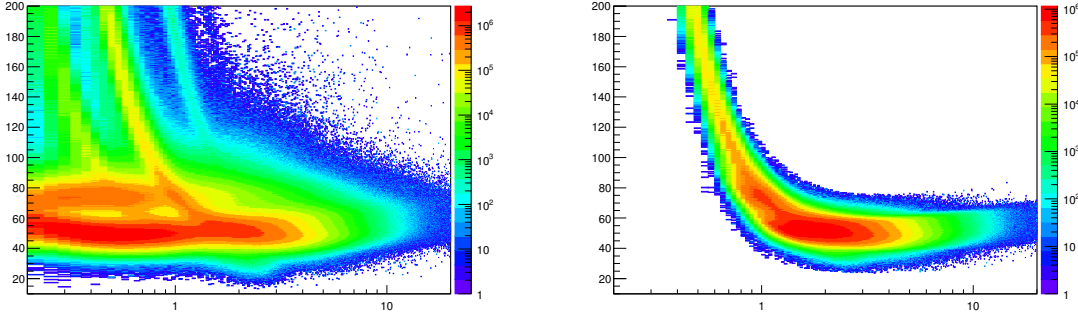


Figure 27: TPC dE/dx as function of transverse momentum for total (top) and selected proton in 3σ (bottom)

835 5.1.4 Signal extraction

836 The Ξ^{*0} signals were reconstructed by invariant-mass analysis of candidates for the decay
 837 products in each transverse momentum interval of the resonance particle, and for each
 838 multiplicity class. The $\Xi^-\pi^+(\Xi^+\pi^-)$ invariant mass distribution is reported in Figure 5.1.4
 839 for semi-central events (20-40%) in p-Pb collisions and Figure 5.1.4 for central events(0-
 840 10%) in Pb-Pb collisions.

841 Since the resonance decay products originate from a position which is indistinguishable
 842 from the PV, a significant combinatorial background is present. In order to extract
 843 $\Xi(1530)^0$ signal it is necessary to remove or, at least reduce, the combinatorial background.
 844 For this analysis, this has been done with the event mixing (EM) technique, by combining
 845 uncorrelated decay products 20 different events in p-Pb (5 different events in Pb-Pb). The
 846 events for the mixing have been selected by applying the similarity criteria to minimise
 847 distortions due to different acceptances and to ensure a similar event structure, only tracks
 848 from events with similar vertex positions z ($|\Delta z| < 1$ cm) and track multiplicities n ($|\Delta n| <$
 849 10) were taken.

850 The mixed-event background distributions were normalised to two fixed regions,
 851 $1.49 < M_{\Xi\pi} < 1.51 \text{ GeV}/c^2$ and $1.56 < M_{\Xi\pi} < 1.58 \text{ GeV}/c^2$, around the Ξ^{*0} mass
 852 peak (Figure 5.1.4 and 5.1.4). These regions were used for all p_T intervals and multiplicity
 853 classes, because the background shape is reasonably well reproduced in these regions and
 854 the invariant-mass resolution of the reconstructed peaks appears stable, independently of
 855 p_T . The uncertainty on the normalisation was estimated by varying the normalisation
 856 regions and is included in the quoted systematic uncertainty for the signal extraction (Section 5.4).

858 After the background subtraction, the resulting distribution is shown in Figure 5.1.4
 859 and 5.1.4. In order to obtain raw yields, a combined fit of a first-order polynomial for

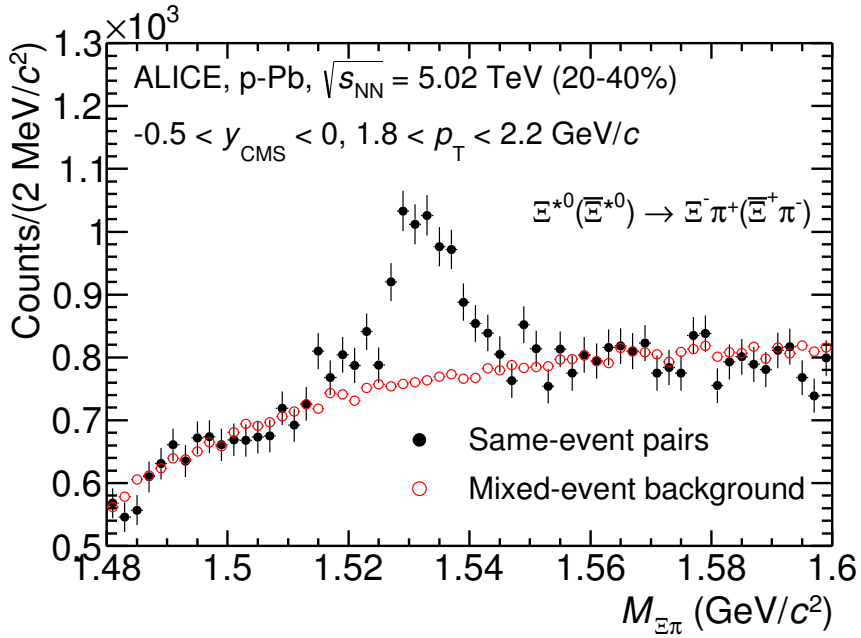


Figure 28: The $\Xi^\pm\pi^\pm$ invariant mass distribution (Same-event pairs) in $1.8 < p_T < 2.2 \text{ GeV}/c$ and for the multiplicity class 20-40%. The background shape, using pairs from different events (Mixed-event background), is normalised to the counts in $1.49 < M_{\Xi\pi} < 1.51 \text{ GeV}/c^2$ and $1.56 < M_{\Xi\pi} < 1.58 \text{ GeV}/c^2$.

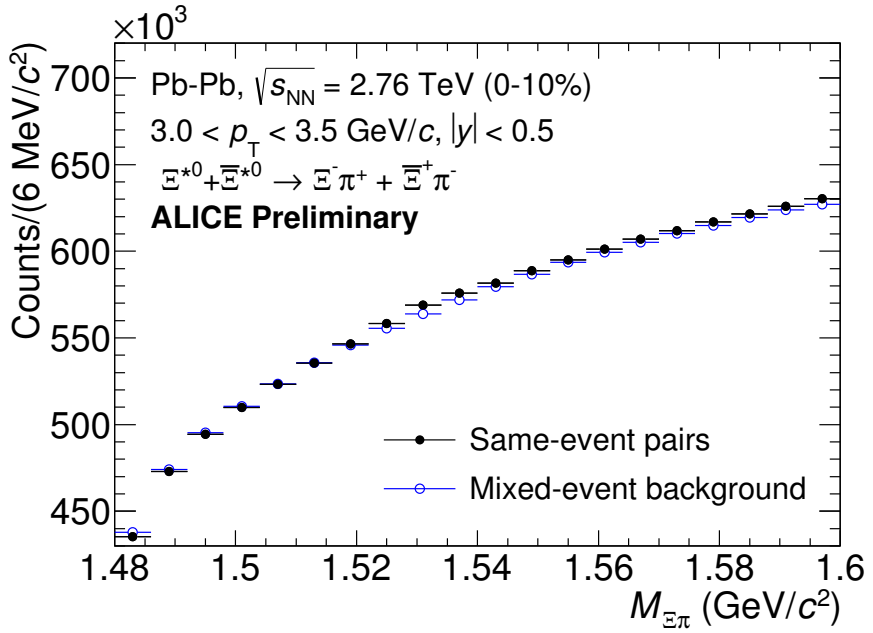


Figure 29: The $\Xi^\pm\pi^\pm$ invariant mass distribution (Same-event pairs) in $3.0 < p_T < 3.5$ GeV/c and for the centrality class 0-10%. The background shape, using pairs from different events (Mixed-event background), is normalised to the counts in $1.49 < M_{\Xi\pi} < 1.51$ GeV/c² and $1.56 < M_{\Xi\pi} < 1.58$ GeV/c².

860 the residual background and a Voigtian function (a convolution of a Breit-Wigner and a
 861 Gaussian function accounting for the detector resolution) for the signal was used. The
 862 mathematical form of fit function used in analysis is:

$$f(M_{\Xi\pi}) = \frac{Y}{2\pi} \frac{\Gamma_0}{(M_{\Xi\pi} - M_0)^2 + \frac{\Gamma_0^2}{4}} \frac{e^{-(M_{\Xi\pi} - M_0)/2\sigma^2}}{\sigma\sqrt{2\pi}} + bg(M_{\Xi\pi}) \quad (10)$$

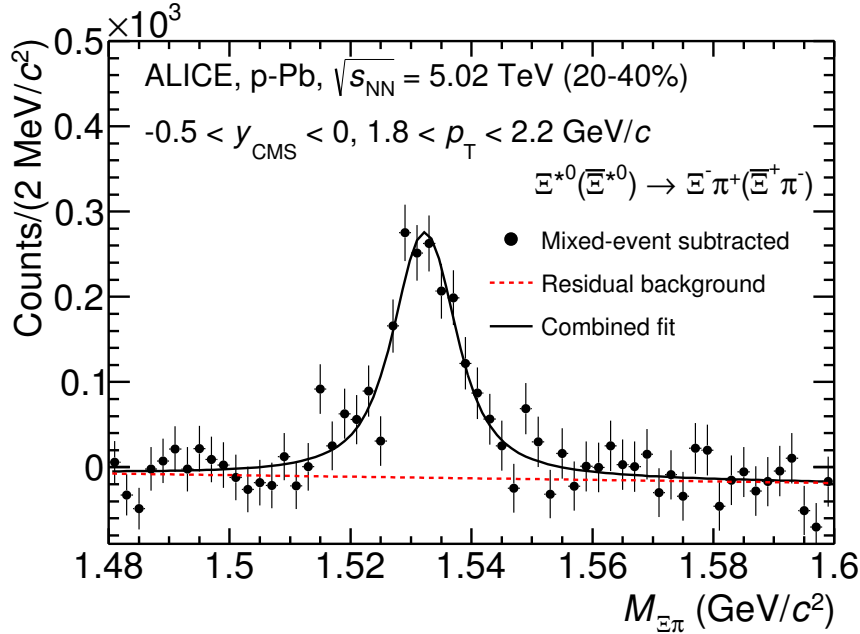


Figure 30: The invariant mass distribution after subtraction of the mixed-event background in p–Pb collisions. The solid curve represents the combined fit, while the dashed line describes the residual background.

863 The mass parameter of the Voigtian fit (M_0) is left free within the fit range ($1.48 \text{ GeV}/c^2$
 864 and $1.59 \text{ GeV}/c^2$). The overall invariant mass width of the Voigtian function is governed
 865 by 2 parameters: σ and Γ_0 . The σ describes the broadening of the peak due to finite
 866 detector resolution while Γ describes the intrinsic width of the resonance itself. The Γ_0 is
 867 fixed to the PDG value of $9.1 \text{ MeV}/c$ for the $\Xi(1530)^0$. Because of lack of statistics, the
 868 σ can be over estimated. Therefore the σ parameter is fixed to value derived from σ in
 869 MB events which has largest statistics. The σ as function of p_T distribution in MB events
 870 is shown in Figure. 32 and we also report invariant mass of $\Xi(1530)^0$ as function of p_T in
 871 Figure. 33. The $\Xi(1530)^0$ raw yields have been extracted from the fit for the 4 multiplicity

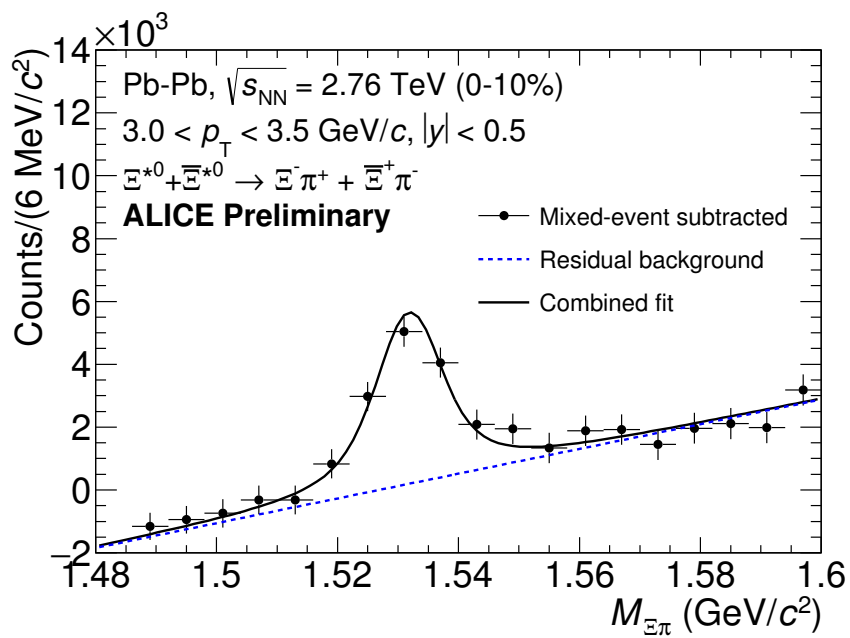


Figure 31: The invariant mass distribution after subtraction of the mixed-event background in Pb–Pb collisions. The solid curve represents the combined fit, while the dashed line describes the residual background.

⁸⁷² bins (+ NSD events) in p–Pb and 4 centrality bins in Pb–Pb collisions and the yields as
⁸⁷³ function of p_T are shown in Figure 34.

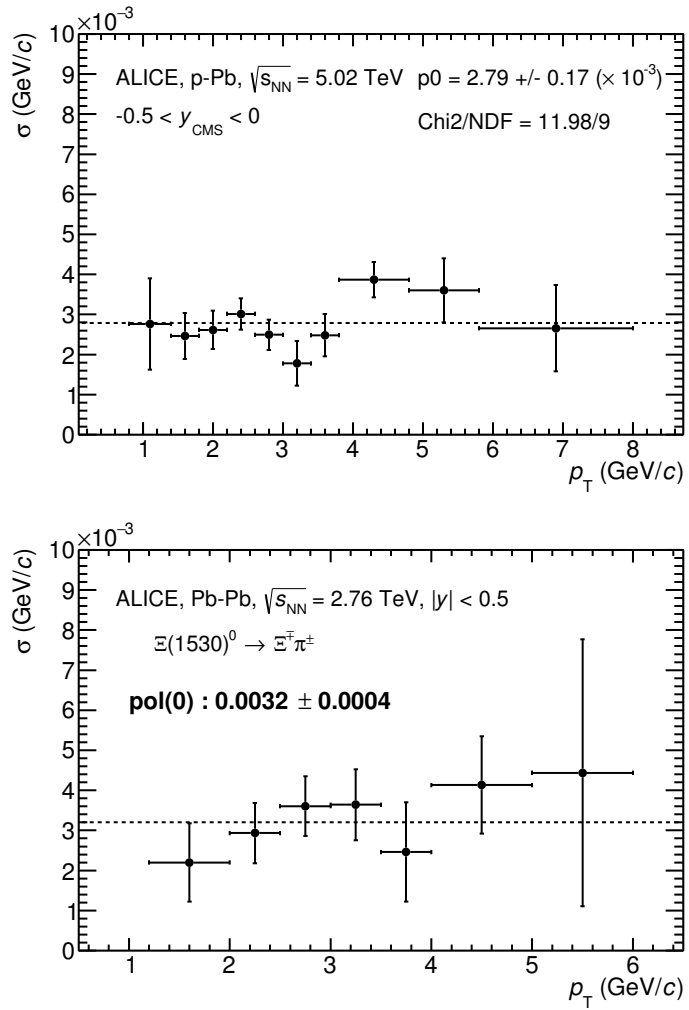


Figure 32: σ fit parameters as a function of p_T in MB in p–Pb collisions (top) and in Pb–Pb collisions (bottom).

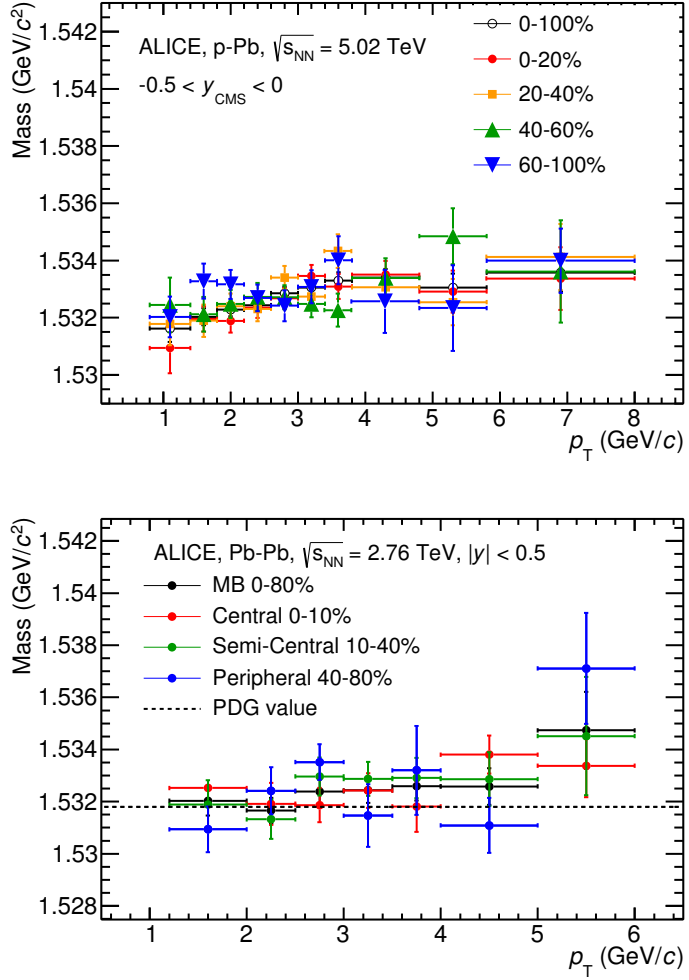


Figure 33: $\Xi(1530)^0$ -mass obtained from fit of the Voigtian peak as a function of p_T in each multiplicity classes in p-Pb collisions (top) and the different centrality classes in Pb-Pb (bottom).

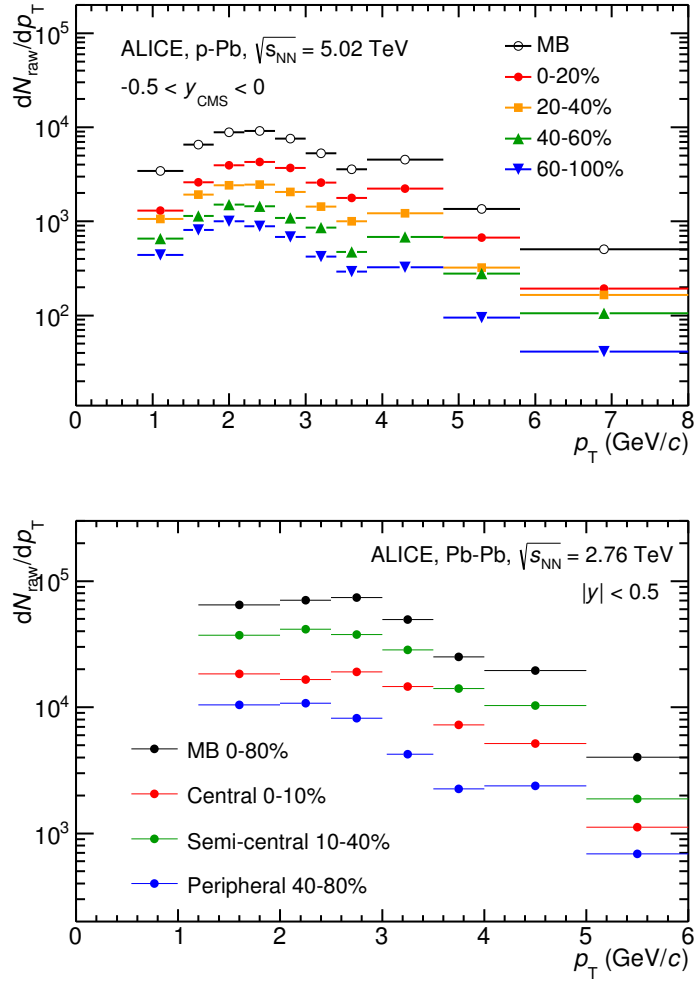


Figure 34: $\Xi(1530)^0$ -raw spectra obtained from fit of the Voigtian peak and a polynomial residual background for different multiplicities in p-Pb collisions (top) and Pb-Pb collisions (bottom). Only the statistical error is reported.

874 **5.2 Efficiency correction**

875 The raw yields were corrected for the geometrical acceptance and the reconstruction effi-
 876 ciency ($A \times \epsilon$) of the detector (Figure. 35). By using the DPMJET 3.05 event generator [37]
 877 and the GEANT 3.21 package [38], a sample of about 100 million p–Pb events was sim-
 878 ulated and reconstructed in order to compute the corrections. The distributions of $A \times \epsilon$
 879 were obtained from the ratio between the number of reconstructed Ξ^{*0} and the number of
 880 generated particle in the same p_T and rapidity interval. Since the correction factors for
 881 different multiplicity classes are in agreement with those from MB events within statistical
 882 uncertainty, the latter were used for all multiplicity classes.

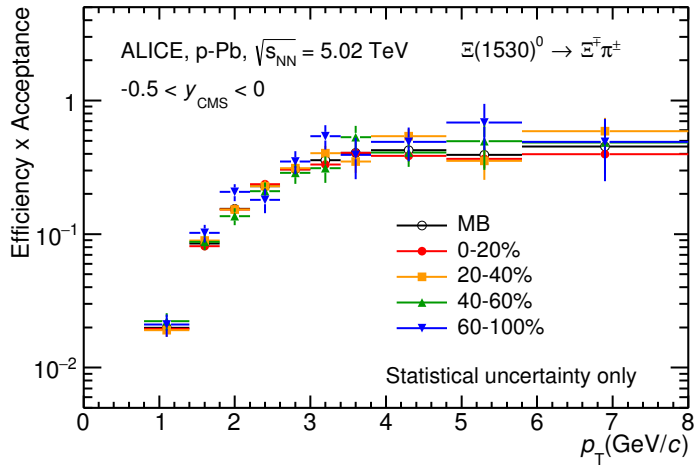


Figure 35: $\Xi(1530)^0$ -raw spectra obtained from fit of the Voigtian peak and a polynomial residual background for different multiplicities. Only the statistical error is reported.

883 Because the generated $\Xi(1530)^0$ spectra have different shapes than the measured $\Xi(1530)^0$
 884 spectra, it is necessary to weight the generated and reconstructed $\Xi(1530)^0$ spectra in these
 885 simulations. Fig. 36 shows the generated and reconstructed $\Xi(1530)^0$ spectra plotted with
 886 the (corrected) measured $\Xi(1530)^0$ spectrum for MB events and the Levy fit of that mea-
 887 sured spectrum. The generated and measured $\Xi(1530)^0$ spectra have different behaviours
 888 for the range $0.5 < p_T < 1$ GeV/ c . The generated $\Xi(1530)^0$ spectrum decreases with
 889 increasing p_T over this range, while the fit of the measured $\Xi(1530)^0$ spectrum reaches a
 890 local maximum in this range. The correction ϵ is observed to change rapidly over this
 891 p_T range. It is therefore necessary to weight the generated spectrum so that it has the
 892 shape of the measured $\Xi(1530)^0$ spectrum (and to apply corresponding weights to the re-
 893 constructed $\Xi(1530)^0$ spectrum). An iterative procedure is performed to determine the
 894 correct weighting (and therefore the correct ϵ).

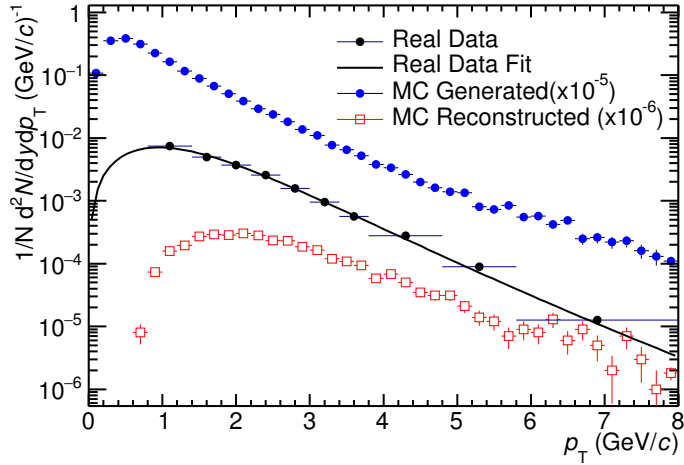


Figure 36: Real corrected $\Xi(1530)^0$ spectrum (black) for the minimum bias with Levy fit (black curve). Also shown are the unweighted generated (blue) and reconstructed (red) $\Xi(1530)^0$ spectra.

- 895 1. The unweighted ϵ is calculated.
- 896 2. This ϵ is used to correct the measured xis spectrum.
- 897 3. The corrected $\Xi(1530)^0$ spectrum is fit.
- 898 4. This fit is used to weight the simulated xis spectra. A p_T dependent weight is applied
899 to the generated xis spectrum so that it follows the fit. The same weight is applied
900 to the reconstructed xis spectrum.
- 901 5. The (weighted) ϵ is calculated.
- 902 6. Steps 2-5 are repeated (with the weighted ϵ from step 5 used as the input for step 2)
903 until the ϵ values are observed to change by $< 0.1\%$ (relative) between iterations. It
904 is observed that four iterations are sufficient for this procedure to converge.

905 Finally, the re-weighted efficiency is obtained and the distribution as function of p_T is
906 shown in Figure 37.

907 In order to obtain the correction factor dedicated in Pb-Pb collisions, MC events are
908 generated using Heavy Ion Jet Interaction Generator (HIJING). The generated events are
909 passed through a GEANT3 model of the ALICE experiment with a realistic description of
910 the detector response. Because we have observed centrality dependent efficiency, the cen-
911 trality dependent efficiencies have been applied to get corrected raw yield. The reweighting

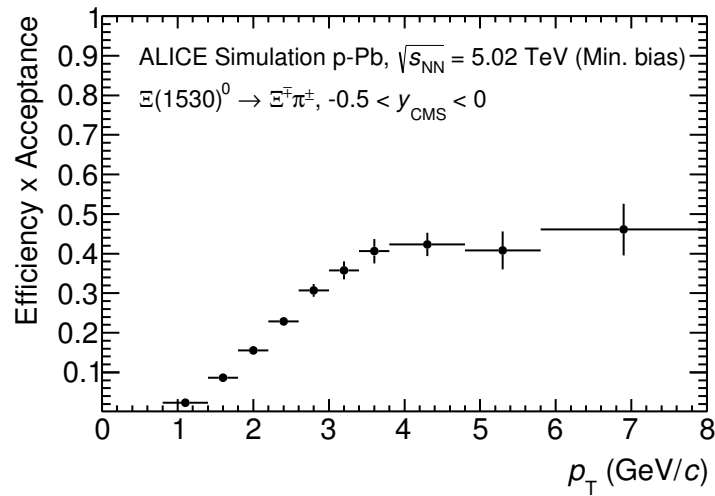


Figure 37: Efficiency as a function of p_T in minimum bias events in p–Pb collisions.

912 approach which was used to correct the efficiency in p–Pb is also applied to the efficiency
 913 obtained in Pb–Pb.

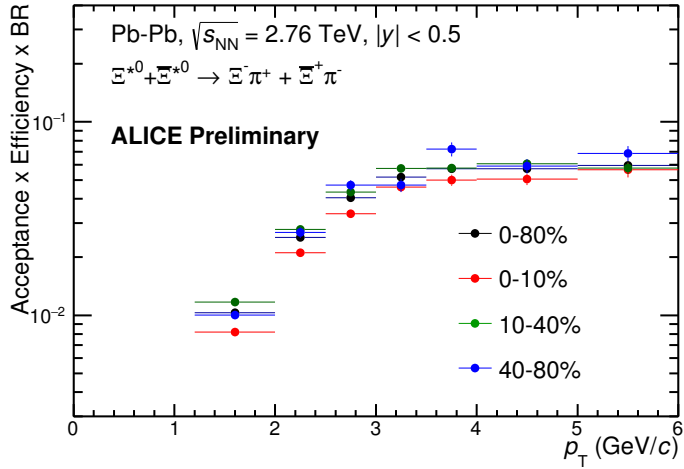


Figure 38: Efficiency as a function of p_T in different centrality classes in Pb–Pb collisions

914 5.3 Corrected p_T -spectra

915 The p_T spectrum is by the number of produced particles of a given type in the desired
 916 interval of phase-space divided by the number of inelastic collisions. The spectrum is
 917 calculated as:

$$\frac{1}{N} \times \frac{d^2N}{dydp_T} = \frac{1}{N_{E,PhysSel}} \times \frac{N_{raw}}{dp_T dy} \frac{1}{\epsilon} \frac{N_{total}^{MC}}{N_{post-PVcut}^{MC}}, \quad (11)$$

918 where N_E represent the number inelastic collisions, the $\frac{dN}{dydp_T}$ is the yield per range of
 919 rapidity y , per range in p_T . On the right hand side $N_{E,PhysSel}$ is the number of events
 920 counted by the physics selection trigger. N_{raw} is the raw extracted number of particle in the
 921 rapidity and p_T bin of width $\Delta y = 0.5$ in p–Pb ($\Delta y = 1.0$ in Pb–Pb) and Δp_T , respectively.
 922 ϵ is the reconstruction efficiency estimated from Monte Carlo simulations. $\frac{N_{total}^{MC}}{N_{post-PVcut}^{MC}}$ is the
 923 ratio of the total number of particle from MC divided by the number of particle from MC
 924 after the Primary-Vertex cut is imposed. It takes into account the fraction of particle lost
 925 after imposing the PV cut. We notice that for minimum-bias results in p–Pb, we adopted
 926 a normalisation such that to provide result from non-single diffractive(NSD) cross-section.
 927 The normalisation factor is 0.964 [5]. The obtained spectrum at MB and the spectrums
 928 from different multiplicity classes in p–Pb are shown in Figure 39 and different centrality
 929 classes in Pb–Pb are shown in Figure 40.

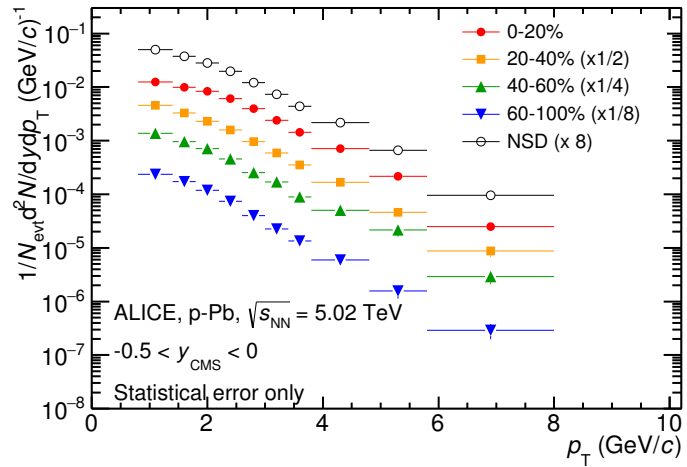


Figure 39: Corrected p_T -spectra of $\Xi(1530)^0$ in NSD and different multiplicity classes in p-Pb collisions.

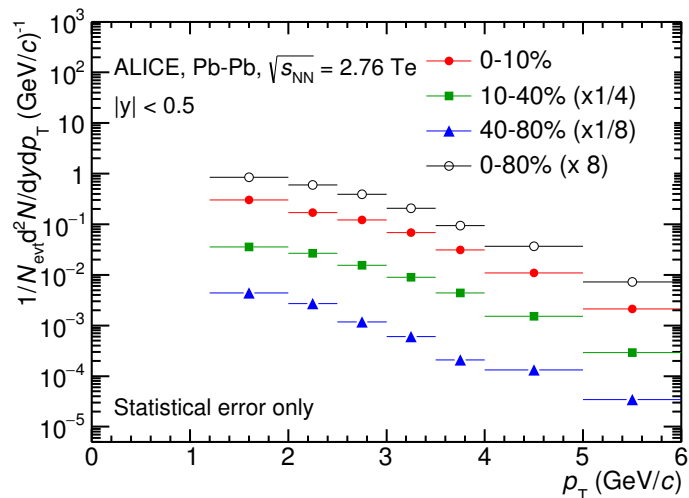


Figure 40: Corrected p_T -spectra of $\Xi(1530)^0$ in different centrality classes in Pb-Pb collisions.

930 **5.4 Systematic uncertainties**

931 The systematic uncertainties are calculated in seven principle groups. The procedure to ob-
 932 tain the systematic uncertainties is performed many times by varying the possible permuta-
 933 tion of the analysis parameter. The general strategy for evaluating systematic uncertainties
 934 is described as following:

- 935 1. Choose one set of parameters for the analysis as default
- 936 2. Observe the deviation of yield when one parameter is changed
- 937 3. The systematic uncertainty is calculated for a given source as the RMS deviation of
 938 the available sources.
- 939 4. The total systematic uncertainty, taking into account all the different sources, is the
 940 sum in quadrature of each source.

941 To study the systematic effect we repeat the measurement by varying one parameter at
 942 a time. A Barlow [39] check has been performed for each measurement to verify whether it
 943 is due to a systematic effect or a statistical fluctuation. Let each measurement be indicated
 944 by $(y_i \pm \sigma_i)$ and the central value (default measurement) by $(y_c \pm \sigma_c)$, one can define $\Delta\sigma_i$
 945 (Eq. 12).

$$\Delta\sigma_i = \sqrt{(|\sigma_i^2 - \sigma_c^2|)} \quad (12)$$

946 Then we calculate $n_i = \Delta y_i / \Delta\sigma_i$, where $\Delta y_i = |y_c - y_i|$. If $n_i \leq 1.0$ then the effects
 947 are due to the statistical fluctuation and if $n_i > 1.0$ we apply consistency check. Since
 948 the alternate and default measurements are not statistically independent, an alternate
 949 measurement which is statistically consistent with the default measurement should not be
 950 used in calculating a systematic uncertainty. The difference between the two measurements
 951 is $\Delta = y_c - y_i$. The difference in quadrature of the uncertainties is calculated by Eq. 12. It
 952 could be possible to check if $\Delta < \sigma$ and exclude such cases from the systematic uncertainties.
 953 However, there can be statistical fluctuations for which $\Delta > \sigma$. If the variations between the
 954 default and alternate measurements are purely statistical, the distribution of Δ/σ should
 955 be a Gaussian with a mean value that is consistent with zero and a deviation σ consistent
 956 with unity. In this analysis, if the mean value is less than 0.1 and σ is less than 1, the
 957 variation passes the consistency check.

958 Only the measurements which passed the Barlow check ($n_i > 1$) are used to determine
 959 the systematic uncertainty. For measurements $N > 2$, the systematic uncertainty has been
 960 determined as the RMS (eqn. 13) of the available measurements. If $N=2$, the absolute
 961 difference is assigned as systematic uncertainty.

$$\delta y_{syst.} = \sqrt{\frac{1}{N} \sum_i (y_i - \bar{y})^2} \quad (13)$$

962 Here N is the total number of available measurements including y_c and \bar{y} is the average
963 of value of the measurements. The measurement did not pass Barlow check, zero systematic
964 uncertainty has been assigned to the value.

965 By suing the way as explained above, all the main contributions to the systematic un-
966 certainty of particle spectra have been studied. In particular those that comes from signal
967 extraction, topological and kinematical selection cuts, track quality selection and $n\sigma$ TPC
968 PID variation. the meaning of each source of systematic uncertainty studied is described
969 in the following:

970

971 **Signal extraction**

972 We have extracted the signal with varying the yield calculating method which contains
973 the method of signal extraction by integrating the Voigtian fit function and bin counting.
974 We also have varied the normalisation range which is related to the invariant mass region
975 where the mixed events distribution is scaled to subtract the combinatorial background
976 and different background estimator such as Like-Sign distribution and polynomial fit was
977 taken account into the systematic source of signal extraction. The systematic uncertainty
978 from signal extraction is sum in quadrature of three sources.

979

980 **Topological selection**

981 To evaluate the stability of the chosen set of values for the topological cuts, loose and tight
982 cuts have beed defined in order to vary by $\pm 10\%$ respectively. The parameters are changed
983 once at a time. Total systematic uncertainty from topological selection is calculated by
984 summation in quadrature of nine sources.

985

986 **TPC $N_{cluster}$ selection**

987 The selection performed for the daughter tracks of the cascade is that $N_{cluster}$ is larger
988 than 70 and the value has been varied to 60 and 80 in order to estimate the systematic
989 uncertainty due to this selection.

990

991 **TPC dE/dx selection**

992 In order to evaluate any potential effect due to the TPC dE/dx selection (U_{PID}), the N_σ
993 selection was varied with $N = 2.5$ and 3.5 .

994

995 **p_T shape correction**

996 As described in Section 5.2, due to the different shape of the measured and generated
997 $\Xi(1530)^0$ spectra, we have applied reweighing procedure to the generated spectra to have
998 same shape and this correction is added into contributor of systematic uncertainty as
999 p_T shape correction.

1000

1001 **Mass window range selection**

1002 In order to select Ξ^\pm which is daughter particle of $\Xi(1530)^0$, we apply the mass window

1003 ± 7 MeV/ c^2 around $\Xi(1530)^0$ mass on $\Lambda\pi$ invariant mass distribution. The boundaries
1004 has been varied to ± 6 MeV/ c^2 and ± 8 MeV/ c^2 to estimate systematic uncertainty.

1005

1006 Vertex range selection

1007 The distribution of vertex-z is shown in Fig.16. The cut on $|Vz|$ was varied from the nominal
1008 ± 10 cm to ± 9 cm, ± 11 cm.

1009

1010 Material Budget and hadronic cross section

1011 A possible source of uncertainty comes from the description of the material, active (detecting area)
1012 or dead (structure and cable), that the particles cross during their travel in the MC with respect to the real material present in the detector. Such description could
1013 affect the reconstruction efficiency in different aspects (e.g. multiple scattering, energy
1014 loss). The value estimated by Ξ analysis [40] has been used in this study which gives 4%
1015 systematic uncertainty. In case of systematic uncertainty from hadronic cross section, we
1016 have inherited the value studied in previous measurement[41] which amount is 1%.

1018

1019 Tracking efficiency

1020 Systematic uncertainties from tracking efficiency from ITS + TPC combined track were
1021 assigned as 3% in p–Pb and 4% in Pb–Pb collision system.[41]
1022 (<https://twiki.cern.ch/twiki/bin/view/ALICE/TrackingEfficiencyCharged>)

1023

1024 Finally, total systematic uncertainty is sum in quadrature of sources listed above. Figure
1025 41 and Figure 42 show the total systematic uncertainty in minimum bias event and
1026 different multiplicity classes in p–Pb collisions, respectively. Again, Figure 43 and Figure
1027 44 present the total systematic uncertainty in minimum bias event and different centrality
1028 classes in Pb–Pb collisions.

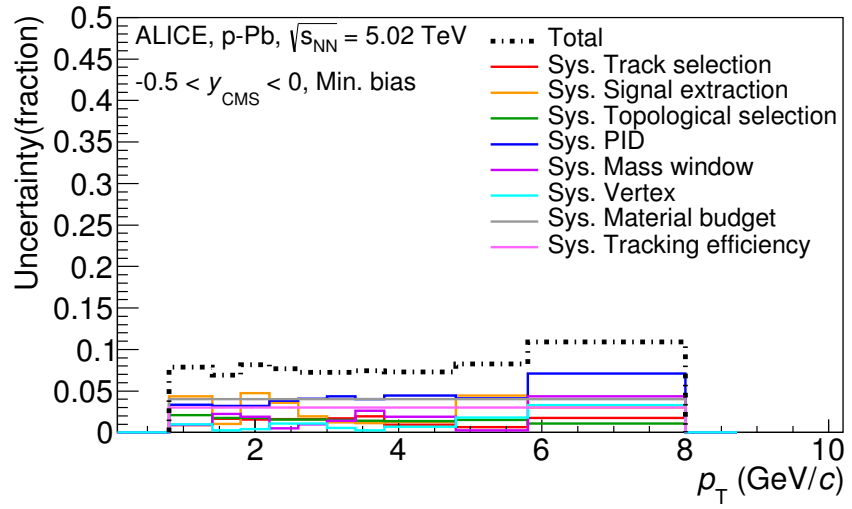


Figure 41: Summary of the contributions to the systematic uncertainty in minimum bias events in p–Pb collisions. The dashed black line is the sum in quadrature of all the contributions.

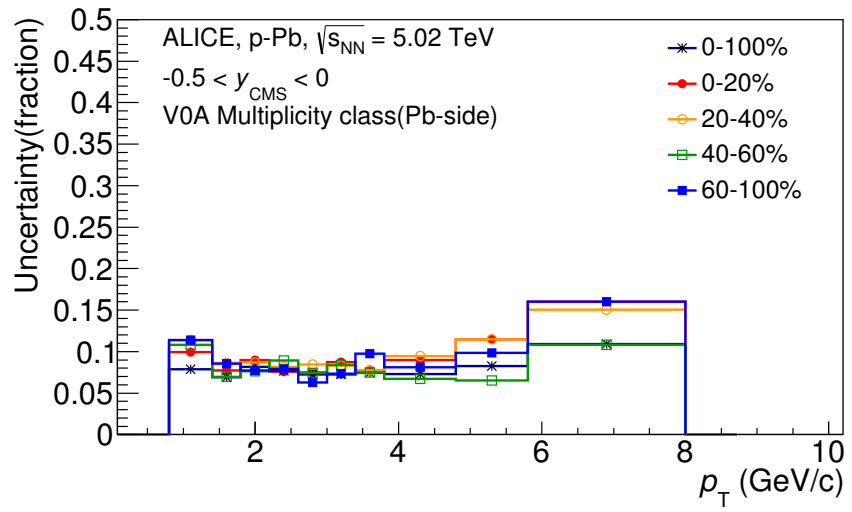


Figure 42: Systematic uncertainties for each multiplicity classes in p–Pb collisions.

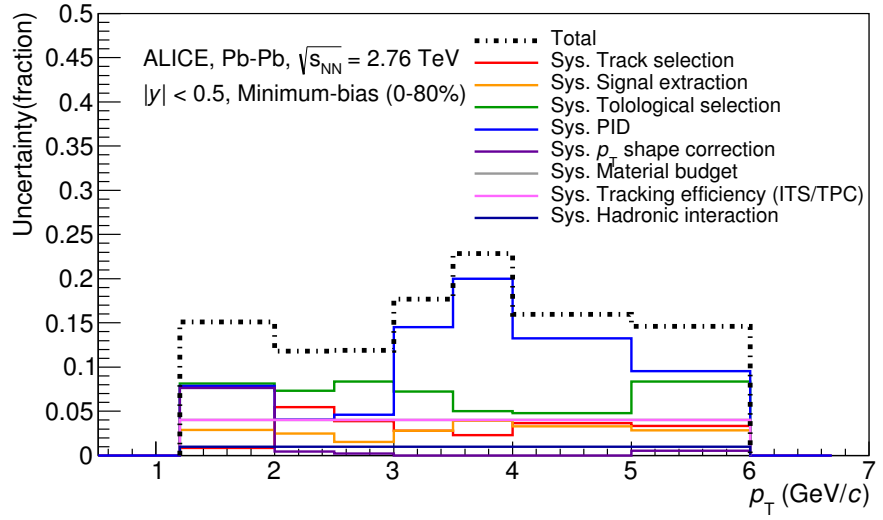


Figure 43: Summary of the contributions to the systematic uncertainty in minimum bias events in Pb–Pb collisions. The dashed black line is the sum in quadrature of all the contributions.

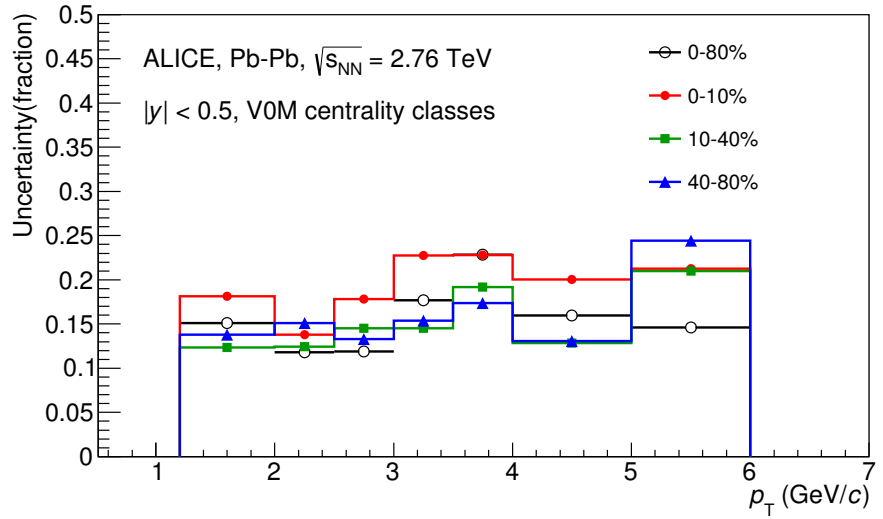


Figure 44: Systematic uncertainties for each multiplicity classes.

Source of uncertainty	p-Pb	Pb-Pb
<i>p</i> _T -dependent		
Tracking efficiency	3%	4%
Tracks selection	1-2%	1-5%
Topological selection	1-2%	5-8%
PID	3-7%	4-20%
Signal extraction	1-5%	1-4%
<i>p</i> _T shape correction	-	0-8%
Mass window (Ξ^\pm)	4%	-
Vertex selection	3%	-
<i>p</i> _T -independent		
Hadronic interaction	-	1%
Material budget	4%	4%
Branching ratio	0.3%	0.3%
Total	8-12%	9-25 %

Table 7: Summary of the systematic uncertainties on the differential yield, $d^2N/(dp_T dy)$. Minimum and maximum values in all p_T intervals and multiplicity classes in p–Pb, centrality classes in Pb–Pb are shown for each source.

1029 **5.5 $\Xi(1530)^0$ transverse momentum spectra**

1030 The raw yield shown in Figure 39 and 40 have been corrected for efficiency as described
 1031 in section 5.2. The measured spectra for $(\Xi(1530)^0 + \bar{\Xi}(1530)^0)/2$ are reported in Figure
 1032 45 for p–Pb collisions and Figure 46 for Pb–Pb collisions. The statistical and systematic
 1033 uncertainties are reported respectively as the error bars and the boxes on the plot. The
 1034 corrected yields for p–Pb collisions are measured with $0.8 < p_T < 8.0$ GeV/c while the
 1035 yields for Pb–Pb collisions are obtained with $1.2 < p_T < 6.0$ GeV/c due to difficulty of
 1036 signal extraction in low and high p_T region.

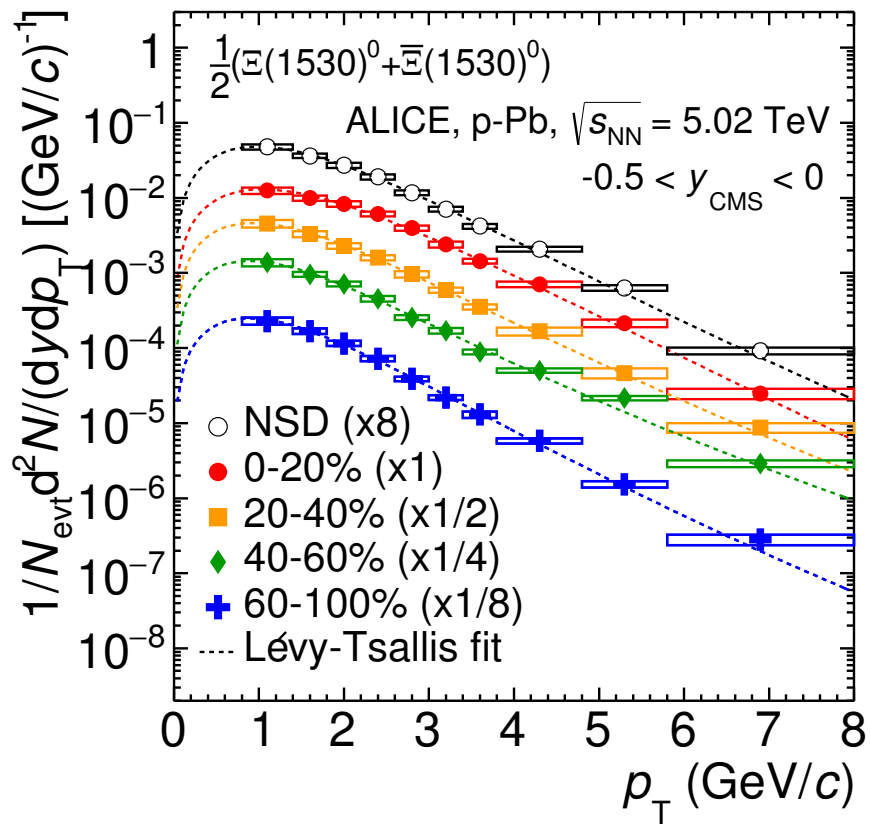


Figure 45: Corrected yields as function of p_T in NSD events and multiplicity dependent event classes in p-Pb collision system. Statistical uncertainties are presented as bar and systematical uncertainties are plotted as boxes.

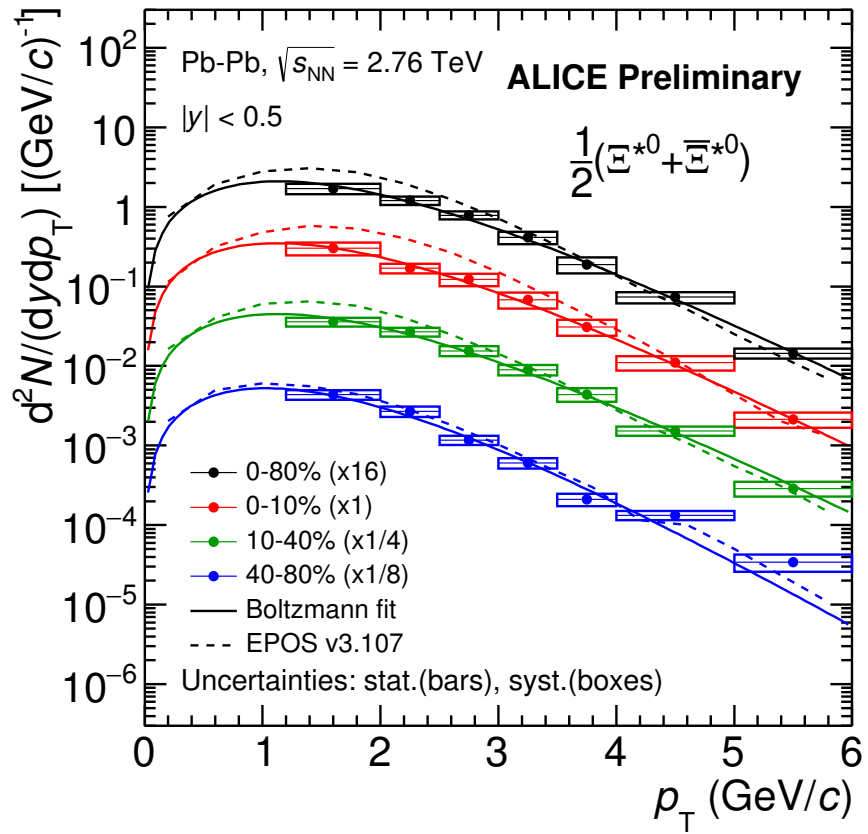


Figure 46: Corrected yields as function of p_T in different centrality classes in Pb–Pb collision system. Statistical uncertainties are presented as bar and systematical uncertainties are plotted as boxes.

1037 6 Further results and discussion

1038 The transverse momentum distributions of double-strange hyperon resonances, $\Xi(1530)^0$
1039 , produced in p–Pb collisions at $\sqrt{s_{\text{NN}}}= 5.02$ TeV and Pb–Pb collisions at $\sqrt{s_{\text{NN}}}= 2.76$
1040 TeV were measured in the mid-rapidity range and they have been already presented in
1041 Chapter 5. From the measurement, the $\langle p_{\text{T}} \rangle$ and integrated particle yield ratios with
1042 system size have been obtained. In the present Chapter these results are compared with
1043 model predictions and discussed in connection with the following topics:

- 1044 • Mean transverse momentum studies
- 1045 • Study of particle production mechanism in hadronic phase
- 1046 • Study of strangeness enhancement

1047 Most of the theoretical aspects related to these topics and, in particular, the description
1048 of the models already have been addressed in Chapter 3.

1049 6.1 Mean transverse momentum

1050 Figure 47 shows the mean transverse momentum $\langle p_{\text{T}} \rangle$ as a function of mean charged-
1051 particle multiplicity density $\langle dN_{\text{ch}}/d\eta_{\text{lab}} \rangle$ at midrapidity. The results for $\Xi(1530)^0$ are
1052 compared with those for other hyperons observed in p–Pb collisions at $\sqrt{s_{\text{NN}}}= 5.02$ TeV [4,
1053 6].

1054 Increasing trends from low to high multiplicities are observed for all hyperons. The
1055 mean transverse momenta increase by 20% as the mean charged-particle multiplicity in-
1056 creases from 7.1 to 35.6. This result is similar to the one obtained for the other hyperons.
1057 Furthermore, a similar increase has been observed also for K^{\pm} , K_S^0 , $K^*(892)^0$ and ϕ [5],
1058 whereas protons are subject to a larger ($\sim 33\%$) increase in the given multiplicity range,
1059 as discussed also in Ref. [4].

1060 In all multiplicity classes, the $\langle p_{\text{T}} \rangle$ follows an approximate mass ordering:

- 1061 • $\langle p_{\text{T}} \rangle_{\Lambda} < \langle p_{\text{T}} \rangle_{\Xi^-} \simeq \langle p_{\text{T}} \rangle_{\Sigma^{*\pm}} < \langle p_{\text{T}} \rangle_{\Xi^{*0}} < \langle p_{\text{T}} \rangle_{\Omega^-}$

1062 The $\langle p_{\text{T}} \rangle$ of $\Sigma^{*\pm}$ looks systematically lower than the $\langle p_{\text{T}} \rangle$ of Ξ^- , despite the larger mass
1063 of $\Sigma^{*\pm}$. The uncertainties, however, are too large to draw any conclusion on possible hints
1064 of violation of the mass hierarchy. This hierarchy of mass-ordering, also including D^0 and
1065 J/ψ in the comparison, is displayed in Figure 48. Note, however, that the D^0 and J/ψ
1066 were measured in different rapidity ranges: $|y_{\text{CMS}}| < 0.5$ [8] ($|y_{\text{CMS}}| < 0.9$ [9]) for D^0 (J/ψ)
1067 in pp and $-0.96 < y_{\text{CMS}} < 0.04$ [8] ($-1.37 < y_{\text{CMS}} < 0.43$ [10]) for D^0 (J/ψ) in p–Pb, and
1068 the results for D^0 and J/ψ in p–Pb collisions are for the 0–100% multiplicity class. This
1069 mass dependence is observed in both p–Pb and pp collisions. It was observed also by the
1070 STAR collaboration [42] in MB pp, MB d–Au and central Au–Au collisions.

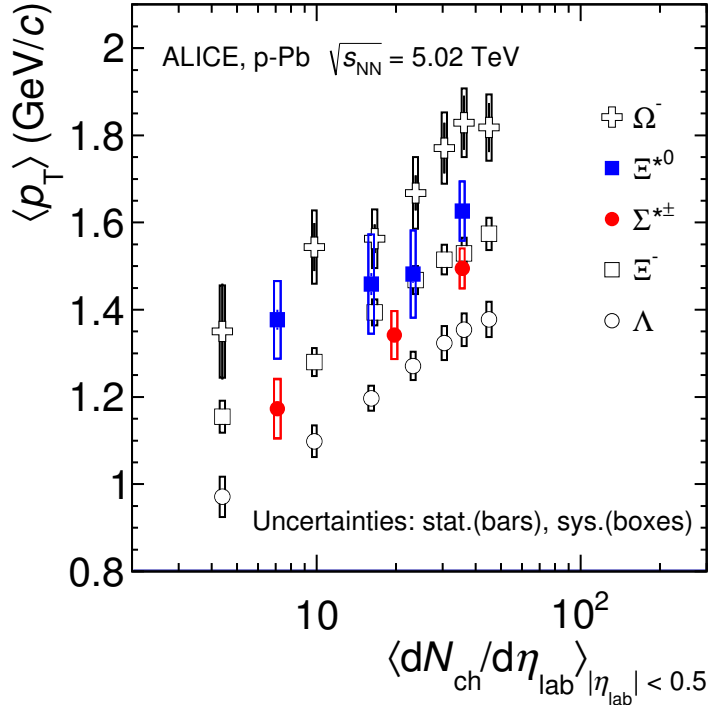


Figure 47: Mean transverse momenta $\langle p_T \rangle$ of Λ , Ξ^- , $\Sigma^{*\pm}$, Ξ^{*0} and Ω^- in p–Pb collisions at $\sqrt{s_{NN}}=5.02$ TeV as a function of mean charged-particle multiplicity density $\langle dN_{ch}/d\eta_{lab} \rangle$, measured in the pseudorapidity range $|\eta_{lab}| < 0.5$. The results for Λ , Ξ^- and Ω^- are taken from [4, 5, 6]. Statistical and systematic uncertainties are represented as bars and boxes, respectively. The Ω^- and Ξ^- points in the 3rd and 4th lowest multiplicity bins are slightly displaced along the abscissa to avoid superposition with the $\Xi(1530)^0$ points.

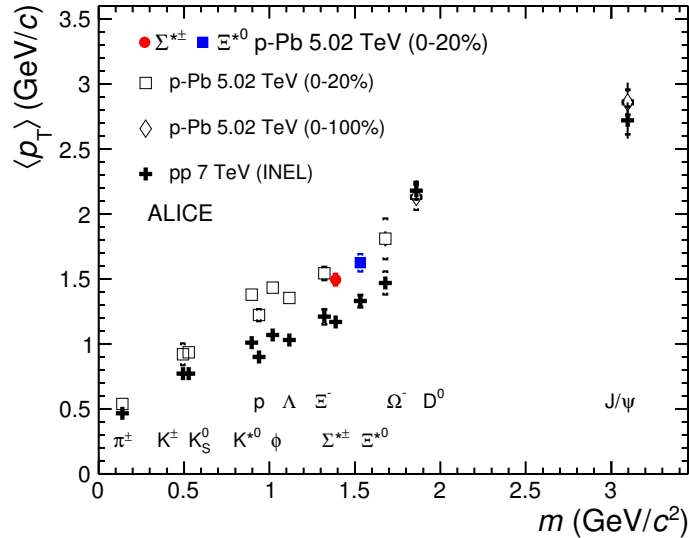


Figure 48: Mass dependence of the mean transverse momenta of identified particles for the 0 – 20% V0A multiplicity class and with $-0.5 < y_{\text{CMS}} < 0$ in p–Pb collisions at $\sqrt{s_{\text{NN}}} = 5.02$ TeV [4, 6], and in minimum-bias pp collisions at $\sqrt{s} = 7$ TeV [7] with $|y_{\text{CMS}}| < 0.5$. Additionally, D^0 and J/ψ results are plotted. The D^0 and J/ψ were measured in different rapidity ranges: $|y_{\text{CMS}}| < 0.5$ [8] ($|y_{\text{CMS}}| < 0.9$ [9]) for D^0 (J/ψ) in pp and $-0.96 < y_{\text{CMS}} < 0.04$ [8] ($-1.37 < y_{\text{CMS}} < 0.43$ [10]) for D^0 (J/ψ) in p–Pb. Note also that the results for D^0 and J/ψ in p–Pb collisions are for the 0–100% multiplicity class.

1071 Furthermore, for the light-flavour hadrons, the mean transverse momenta in p–Pb col-
1072 lisions are observed to be consistently higher than those in pp collisions at 7 TeV. The
1073 situation for the charm hadrons is different, where $\langle p_T \rangle$ appears compatible between both
1074 colliding systems. The discrepancy is likely due to different production mechanisms for
1075 heavy and light flavours and to a harder fragmentation of charm quarks. Specifically, the
1076 fact that $\langle p_T \rangle$ remains similar in pp and in p–Pb is consistent with an $R_{p\text{Pb}}$ ratio com-
1077 patible with unity at all p_T [8] for D^0 , and/or with the effects of shadowing in p–Pb which
1078 reduces the production at low p_T and thus increasing the overall $\langle p_T \rangle$ for J/ψ [10]; the
1079 small p_T hardening expected in pp when going from 5.02 to 7TeV is apparently not enough
1080 to counter-balance the situation.

1081 Because of small decrease of the $\langle p_T \rangle$ for proton and Λ relative to those for K^{*0} and
1082 ϕ , two different trends for mesons and baryons have been suggested [43]. Even including
1083 D^0 and J/ψ , as shown in Figure 48, a different trend for mesons and baryons cannot be
1084 convincingly established.

1085 **6.2 Particle yield ratios**

1086 **6.2.1 Integrated yield ratios of excited to ground-state hadrons**

1087 The integrated yield ratios of excited to ground-state hyperons [44, 4, 7, 6] with the same
1088 strangeness content, for different collision systems and energies, are shown in Figure 49
1089 as a function of system size. The ratio of $\Xi(1530)^0$ to Ξ is flat across the system and
1090 it complements the information derived from other resonance measurement for different
1091 lifetime which are shown in Figure 50.

1092 The short-lived resonances(ρ , K^* and Λ^*) which exhibit suppression from peripheral to
1093 central lead-lead collisions and with respect to thermal model in central lead-lead collisions.
1094 Currently favored explanation of is dominance of elastic re-scattering of decay daughters
1095 over regeneration in the hadronic phase.

1096 The constant behavior of the yield ratios of excited to ground-state hyperons with same
1097 strangeness content ($\Xi(1530)^0$ and Φ) indicates that neither regeneration nor re-scattering
1098 dominates with increasing collision system size because of its longer-lifetime.

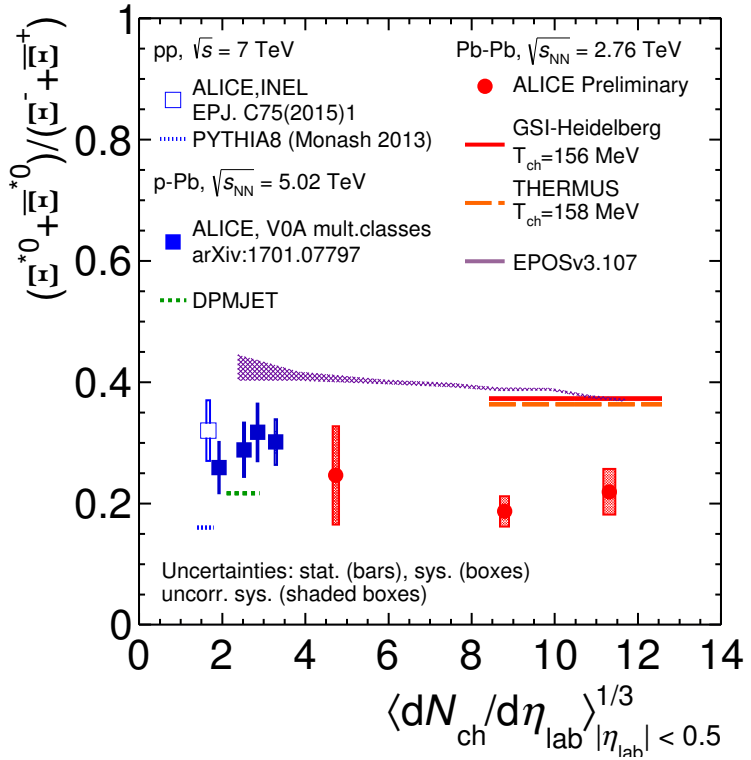


Figure 49: Ratio of $\Xi(1530)^0$ to Ξ^- measured in pp [7], p–Pb [4, 6] and Pb–Pb collisions as a function of $\langle dN_{ch}/d\eta_{lab} \rangle$ measured at midrapidity. Statistical uncertainties (bars) are shown as well as total systematic uncertainties (hollow boxes) and systematic uncertainties uncorrelated across multiplicity (shaded boxes). A few model predictions are also shown as lines at their appropriate abscissa.

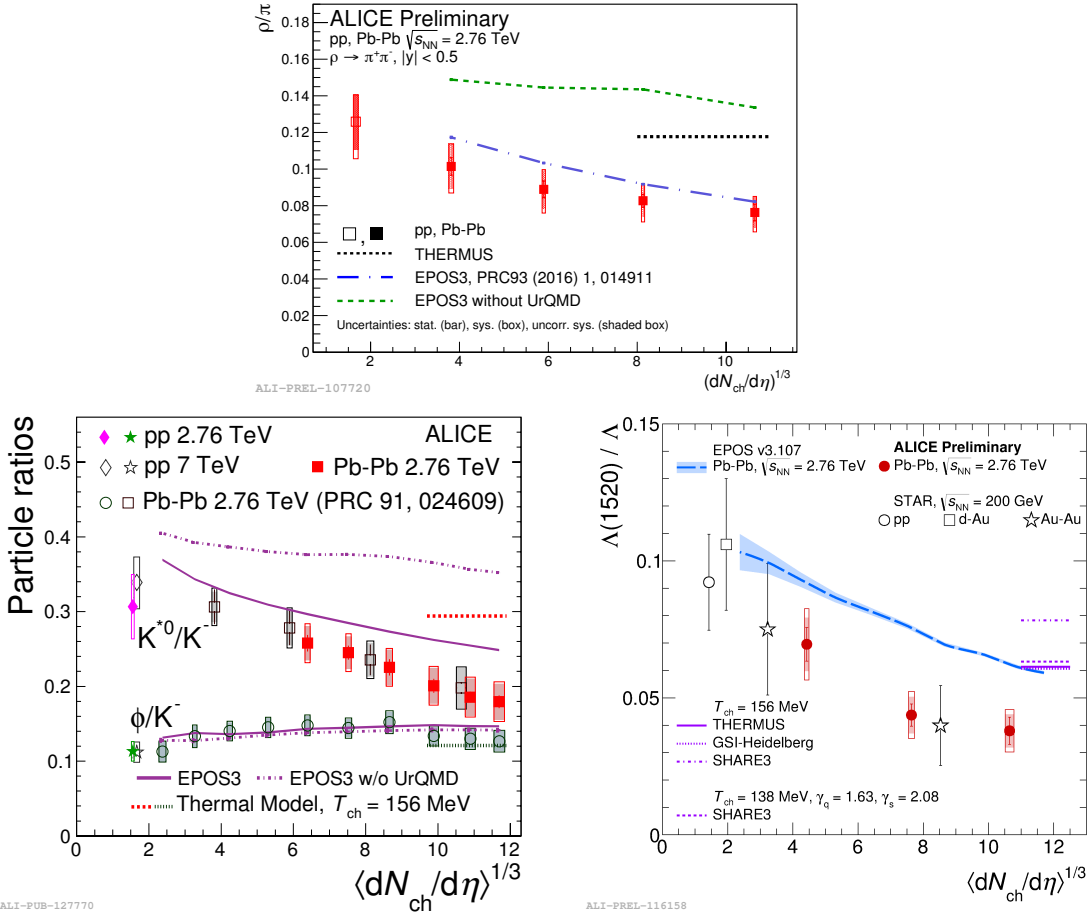


Figure 50: Ratio of ρ/π (Up), K^*/K , ϕ/K (Left bottom) and Λ^*/Λ with system size measured at mid-rapidity. Statistical uncertainties (bars) are shown as well as total systematic uncertainties (hollow boxes) and systematic uncertainties uncorrelated across multiplicity (shaded boxes). A few model predictions are also shown as lines at their appropriate abscissa.

1099 **6.3 Integrated yield ratios to pion**

1100 The integrated yield ratios of excited hyperons to pions are shown in Figure 51 to study
1101 the evolution of relative strangeness production yields with increasing collision system
1102 size. The ratio of $\Xi(1530)^0$ to Ξ is observed to be increase from pp to p–Pb collisions
1103 system and then, decrease from peripheral to central Pb–Pb collision. The QCD-inspired
1104 predictions like PYTHIA for pp [45] and DPMJET for p–Pb [37] clearly underestimate
1105 the observed yield ratios, while the statistical one seems to be comparable with results
1106 from high multiplicity in p–Pb but the ratio in Pb–Pb is below with respect to the model.
1107 The results in pp and p–Pb collisions are consistent with previous observation of ground-
1108 state hyperons to pion ratios. The Figure 52 presents particle yield ratios to pions of
1109 strange and multi-strange hadrons normalized to the values measured in pp collisions. As
1110 shown in the Figure 52, the $\Xi(1530)^0$ to pion ratios follow the trend of $\Xi \pi$ as function of
1111 $\langle dN_{ch}/d\eta_{lab} \rangle$ and indicate that the strangeness enhancement observed in p–Pb collisions
1112 depends predominantly on the strangeness content, rather than on the hyperon mass.

1113 The Figure 53 also shows the hyperon-to-pion ratios and compared with model predic-
1114 tions. The

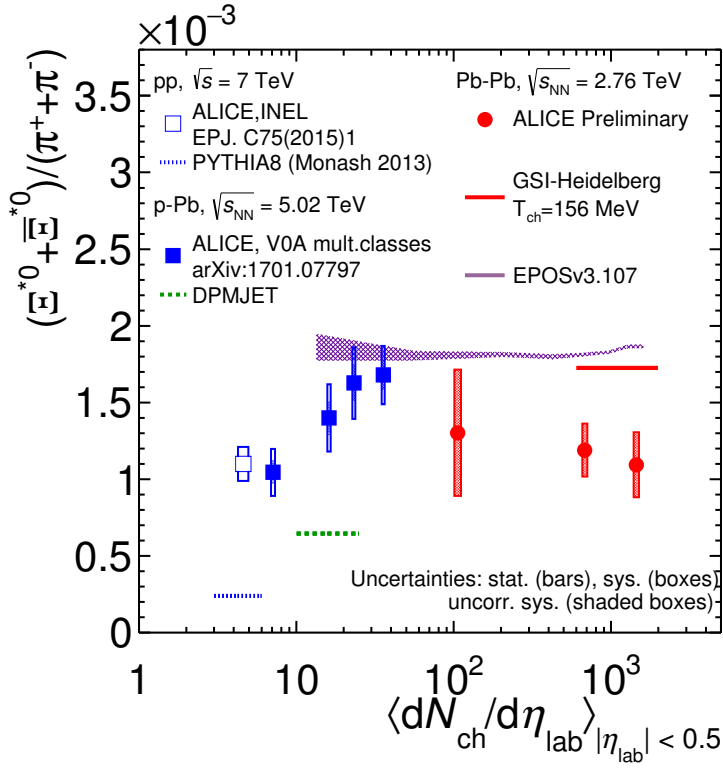


Figure 51: Ratio of $\Xi(1530)^0$ to π^\pm , measured in pp [11] and p–Pb [7] collisions, as a function of the average charged particle density ($\langle dN_{ch}/d\eta_{lab} \rangle$) measured at mid-rapidity. Statistical uncertainties (bars) are shown as well as total systematic uncertainties (hollow boxes) and systematic uncertainties uncorrelated across multiplicity (shaded boxes). A few model predictions are also shown as lines at their appropriate abscissa.

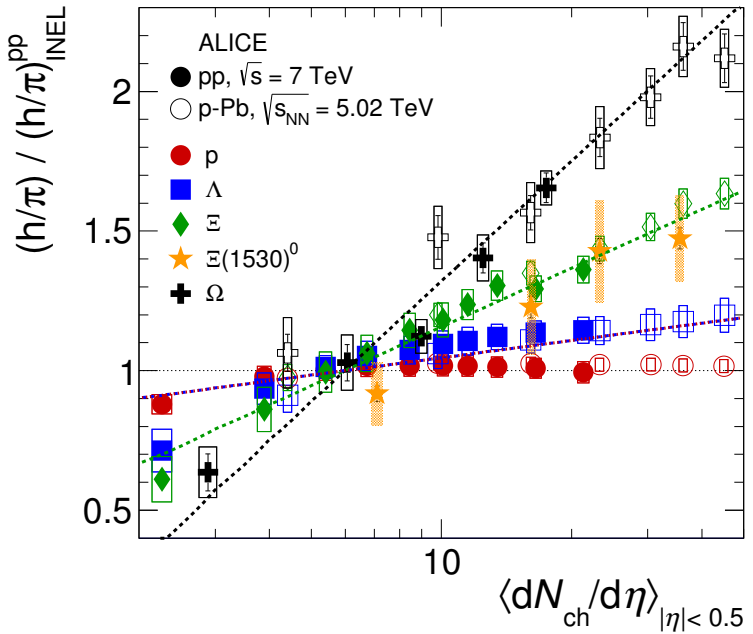


Figure 52: Particle yield ratios to pions of strange and multi-strange hadrons normalized to the values measured in pp collisions, both in pp and in p -Pb collisions. The common systematic uncertainties cancel in the double-ratio. The empty boxes represent the remaining uncorrelated uncertainties. The lines represent a simultaneous fit of the results with the empirical scaling formula in Equation ??.

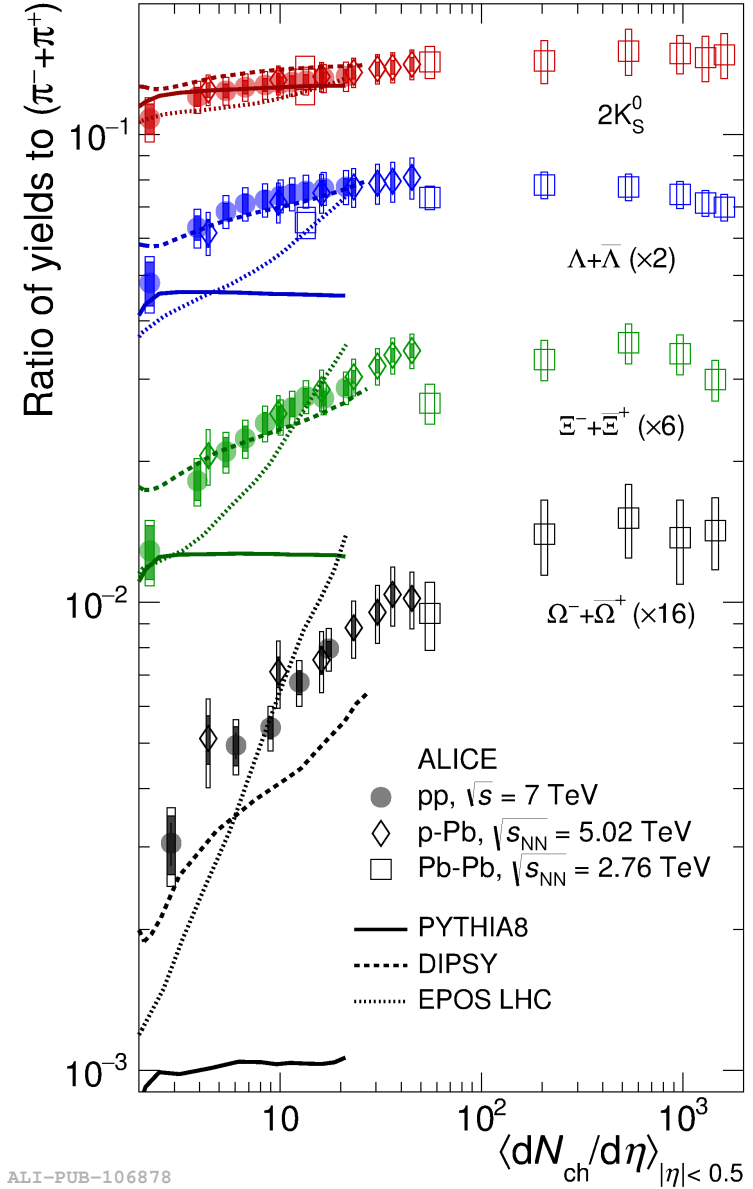


Figure 53: p_T -integrated yield ratios of strange and multi-strange hadrons to $(\pi^+ + \pi^-)$ as a function of $\langle dN_{ch}/d\eta_{lab} \rangle$ measured in the rapidity interval $|\eta| < 0.5$. The empty and dark-shaded boxes show the total systematic uncertainty and the contribution uncorrelated across multiplicity bins, respectively. The values are compared to calculations from MC models and to results obtained in Pb–Pb and p–Pb collisions at the LHC.

1115 **References**

- 1116 [1] **Particle Data Group** Collaboration, K. Olive *et al.*, “Review of Particle Physics,”
1117 *Chin. Phys. C* **38** (2014) 090001.
- 1118 [2]
- 1119 [3] **ALICE** Collaboration, K. e. a. Aamodt, “Alignment of the ALICE Inner Tracking
1120 System with cosmic-ray tracks,” *JINST* **5** (2010) P03003.
- 1121 [4] **ALICE** Collaboration, J. Adam *et al.*, “Multiplicity dependence of pion, kaon,
1122 proton and lambda production in p–Pb collisions at $\sqrt{s_{\text{NN}}}= 5.02 \text{ TeV}$,” *Phys. Lett.*
1123 **B728** (2014) 25–38, [arXiv:1307.6796 \[nucl-ex\]](#).
- 1124 [5] **ALICE** Collaboration, J. Adam *et al.*, “Production of $K^*(892)^0$ and $\phi(1020)$ in
1125 p–Pb collisions at $\sqrt{s_{\text{NN}}}= 5.02 \text{ TeV}$,” *Eur. Phys. J. C* **76** (2016) 245,
1126 [arXiv:1601.7868 \[nucl-ex\]](#).
- 1127 [6] **ALICE** Collaboration, J. Adam *et al.*, “Multi-strange baryon production in p–Pb
1128 collisions at $\sqrt{s_{\text{NN}}}= 5.02 \text{ TeV}$,” *Phys. Lett. B* **758** (2016) 389–401,
1129 [arXiv:1512.07227 \[nucl-ex\]](#).
- 1130 [7] **ALICE** Collaboration, B. Abelev *et al.*, “Production of $\Sigma(1385)^{\pm}$ and $\Xi(1530)^0$ in
1131 proton-proton collisions at $\sqrt{s}= 7 \text{ TeV}$,” *Eur. Phys. J. C* **75** (2015) 1,
1132 [arXiv:1406.3206 \[nucl-ex\]](#).
- 1133 [8] **ALICE** Collaboration, J. Adam *et al.*, “ D -meson production in p–Pb collisions at
1134 $\sqrt{s_{\text{NN}}}= 5.02 \text{ TeV}$ and in pp collisions at $\sqrt{s}= 7 \text{ TeV}$,” *Phys. Rev. C* **94** (2016)
1135 054908, [arXiv:1605.07569 \[nucl-ex\]](#).
- 1136 [9] **ALICE** Collaboration, B. Abelev *et al.*, “Inclusive J/ψ production in pp collisions
1137 at $\sqrt{s}= 2.76 \text{ TeV}$,” *Phys. Lett. B* **718** (2012) 295–306, [arXiv:1203.3641 \[hep-ex\]](#).
- 1138 [10] **ALICE** Collaboration, J. Adam *et al.*, “Rapidity and transverse-momentum
1139 dependence of the inclusive J/ψ nuclear modification factor in p–Pb collisions at
1140 $\sqrt{s_{\text{NN}}}= 5.02 \text{ TeV}$,” *JHEP* **06** (2015) 55, [arXiv:1503.07179 \[nucl-ex\]](#).
- 1141 [11] **ALICE** Collaboration, J. Adam *et al.*, “Measurement of pion, kaon and proton
1142 production in proton-proton collisions at $\sqrt{s}= 7 \text{ TeV}$,” *Eur. Phys. J. C* **75** (2015)
1143 226, [arXiv:1504.00024 \[nucl-ex\]](#).
- 1144 [12] F. Halzen and A. Martin.
- 1145 [13] S. Wheaton, J. Cleymans, and M. Hauer, “THERMUS: A Thermal model package
1146 for ROOT,” *Comput. Phys. Commun.* **180** (2009) 84–106, [hep-ph/0407174](#).

- 1147 [14] J. Cleymans, S. Kabana, I. Kraus, H. Oeschler, K. Redlich, and N. Sharma,
 1148 “Antimatter production in proton-proton and heavy-ion collisions at ultrarelativistic
 1149 energies,” *Phys. Rev.* **C84** (2011) 054916, [arXiv:1105.3719 \[hep-ph\]](#).
- 1150 [15] L. Evans and P. Bryant.
- 1151 [16]
- 1152 [17]
- 1153 [18]
- 1154 [19]
- 1155 [20]
- 1156 [21]
- 1157 [22] **ALICE** Collaboration, K. Aamodt *et al.*, “The ALICE experiment at the CERN
 1158 LHC,” *JINST* **3** (2008) S08002.
- 1159 [23] **ALICE** Collaboration, L. B. et al, “Definition of the ALICE coordinate system and
 1160 basic rules for sub-detector components numbering,” *In Internal Note
 1161 ALICE-INT-2003-038* .
- 1162 [24] **ALICE** Collaboration, J. e. a. Alme, “The ALICE TPC, a large 3-dimensional
 1163 tracking device with fast readout for ultra-high multiplicity events,” *In Nuclear
 1164 Instruments and Method in Physics Research* **A622** (2010) 316–367.
- 1165 [25]
- 1166 [26] R. Glauber.
- 1167 [27] A. S. K.C. Chung, C.S. Whang and G. Pech.
- 1168 [28] **ALICE** Collaboration, J. Adam *et al.*, “Centrality dependence of particle
 1169 production in p–Pb collisions at $\sqrt{s_{\text{NN}}}= 5.02 \text{ TeV}$,” *Phys. Rev.* **C91** (2015) 064905,
 1170 [arXiv:1412.6828 \[nucl-ex\]](#).
- 1171 [29] **ALICE** Collaboration, B. Abelev *et al.*, “Centrality determination of Pb–Pb
 1172 collisions at $\sqrt{s_{\text{NN}}}= 2.76 \text{ TeV}$ with ALICE,” *Phys. Rev.* **C88** (2013) ,
 1173 [arXiv:1303.0737 \[nucl-ex\]](#).
- 1174 [30]
- 1175 [31]

- 1176 [32] e. a. Bagnasco. S.
- 1177 [33] R. Brun and F. Rademakers.
- 1178 [34] **ALICE** Collaboration, B. Abelev *et al.*, “Performance of the ALICE Experiment at
1179 the CERN LHC,” *Int. J. Mod. Phys. A***29** (2014) 1430044, [arXiv:1402.4476](#)
1180 [nucl-ex].
- 1181 [35] **ALICE** Collaboration, B. Abelev *et al.*, “Pseudorapidity Density of Charged
1182 Particles in p–Pb Collisions at $\sqrt{s_{\text{NN}}}=5.02$ TeV,” *Phys. Rev. Lett.* **110** (2013)
1183 032301, [arXiv:1210.3615](#) [nucl-ex].
- 1184 [36] **ALICE** Collaboration, K. Aamodt *et al.*, “Strange particle production in
1185 proton-proton collisions at $\sqrt{s}=0.9$ TeV with ALICE at the LHC,” *Eur. Phys. J.*
1186 **C71** (2011) 1594, [arXiv:1012.3257](#) [nucl-ex].
- 1187 [37] S. Roesler, R. Engel, , and J. Ranft, “The Monte Carlo Event Generator
1188 DPMJET-III, Advanced Monte Carlo for Radiation Physics, Particle Transport
1189 Simulation and Applications,” *Conference Proceedings, MC2000, Lisbon, Portugal,*
1190 *October 23–26* (2000) 1033–1038, [hep-ph/0012252](#).
- 1191 [38] R. Brun, F. Carminati, and S. Giani, “GEANT detector description and simulation
1192 tool,” *CERN-W5013* (1994) .
- 1193 [39] R. Barlow, “Systematic Errors: Facts and Fictions,” *Presented at Advanced
1194 Statistical Techniques in HEP, Durham, March 2002* (2002) 333p,
1195 [hep-ex/0207026v1](#).
- 1196 [40] **ALICE** Collaboration, B. Abelev *et al.*, “Multi-strange baryon production at
1197 mid-rapidity in Pb–Pb collisions at $\sqrt{s_{\text{NN}}}=2.76$ TeV,” *Phys. Lett. B***728** (2014)
1198 216–227, [arXiv:1307.5543](#) [nucl-ex].
- 1199 [41] **ALICE** Collaboration, B. Abelev *et al.*, “Centrality dependence of π , K and p
1200 production in Pb–Pb collisions at $\sqrt{s_{\text{NN}}}=2.76$ TeV,” *Phys. Rev. C***88** (2013) ,
1201 [arXiv:1301.4361](#) [nucl-ex].
- 1202 [42] **STAR** Collaboration, B. I. Abelev *et al.*, “Hadronic resonance production in d–Au
1203 collisions at $\sqrt{s_{\text{NN}}}=200$ GeV measured at the BNL Relativistic Heavy-Ion Collider,”
1204 *Phys. Rev. C***78** (2008) 044906, [arXiv:0801.0450](#) [nucl-ex].
- 1205 [43] A. Velásquez, “Mean p_{T} scaling with m/n_q at the LHC: Absence of (hydro) flow in
1206 small systems?,” *Nucl. Phys. A***943** (2015) 9–17, [arXiv:1506.00584](#) [hep-ph].
- 1207 [44] **ALICE** Collaboration, B. Abelev *et al.*, “Multi-strange baryon production in pp
1208 collisions at $\sqrt{s}=7$ TeV with ALICE,” *Phys. Lett. B***712** (2012) 309,
1209 [arXiv:1204.0282](#) [nucl-ex].

- 1210 [45] T. Sjöstrand, S. Mrenna, and P. Skands, “A brief introduction to PYTHIA 8.1,”
1211 *Comput. Phys. Comm.* **178** (2008) 852–867, arXiv:0710.3820 [hep-ph].

1212 **Acknowledgements**